Characterization Of Low-Frequency Combustion Stability Of The Fastrac Engine[a]

Marvin Rocker
Fluid Physics and Dynamics Group
NASA/Marshall Space Flight Center
Huntsville, Alabama

ABSTRACT:

A series of tests were conducted to measure the combustion performance of the Fastrac engine thrust chamber. During mainstage, the thrust chamber exhibited no large-amplitude chamber pressure oscillations that could be identified as low-frequency combustion instability or “chug”. However, during start-up and shutdown, the thrust chamber very briefly exhibited large-amplitude chamber pressure oscillations that were identified as chug. These instabilities during start-up and shutdown were regarded as benign due to their brevity. Linear models of the thrust chamber and the propellant feed systems were formulated for both the thrust chamber component tests and the flight engine tests. These linear models determined the frequency and decay rate of chamber pressure oscillations given the design and operating conditions of the thrust chamber and feed system. The frequency of chamber pressure oscillations determined from the model closely matched the frequency of low-amplitude, low-frequency chamber pressure oscillations exhibited in some of the later thrust chamber mainstage tests. The decay rate of the chamber pressure oscillations determined from the models indicated that these low-frequency oscillations were stable. Likewise, the decay rate, determined from the model of the flight engine tests indicated that the low-frequency chamber pressure oscillations would be stable.

INTRODUCTION:

NASA’s Marshall Space Flight Center (MSFC) was tasked with developing a 60,000 pound (267,670 N) thrust, pump-fed, LOX/RP-1 engine under the Advanced Space Transportation Program (ASTP). This government-led design has been designated the *Fastrac* engine, illustrated in figure-1.

The X-34[b] vehicle, illustrated in figure-2, was to use the Fastrac engine as the main propulsion system. The X-34 was to be a suborbital vehicle developed by the Orbital Sciences Corporation. The X-34 vehicle was to be launched from an L-1011 airliner. After launch, the X-34 vehicle was to be able to climb to altitudes up to 250,000 feet (76,200 m) and reach speeds up to Mach 8, over a mission range of 500 miles (805 Km). The overall length, wingspan, and gross takeoff weight of the X-34 vehicle were to be 58.3 feet (17.8 m), 27.7 feet (8.4 m) and 45,000 pounds (200,752 N), respectively.

This report summarizes the formulation of the linear model used in the study of the low-frequency combustion stability characteristics of the two Fastrac engine configurations. The first configuration was the Fastrac thrust chamber assembly (TCA) and its propellant feed system at MSFC’s test stand 116. The second configuration was the Fastrac flight engine tested at NASA’s Stennis Space Center (SSC). Also summarized is the Fastrac TCA design, the layout of the propellant feed system at MSFC’s test stand 116, and the low-frequency combustion stability characteristics exhibited by the Fastrac TCA and propellant feed system during testing as was determined from high-frequency chamber pressure measurements.

OBJECTIVE:

One of the objectives of Fastrac TCA testing was to achieve a stable mainstage test that met a criteria for combustion stability as established by JANNAF standards[1]. This criteria was that the amplitude of the chamber pressure oscillations was to be 10% or less of the mean chamber pressure.

---

[a] Approved for public release, distribution is unlimited.

[b] The X-34 project was cancelled by NASA in March, 2001.

Typically, in the context of high-frequency combustion instability, two stardards were to be met. First, the damp time of bomb-induced chamber pressure oscillations was to be 29 milliseconds or less. This damp time was determined from a combustion chamber acoustic frequency for the first-tangential (1T) mode of 1922 Hz. Second, the amplitude of the chamber pressure oscillations was to be 10% or less of the mean chamber pressure after the bomb-induced chamber pressure oscillations damped out. Both of these criteria were met during bomb testing whereby the high-frequency combustion instabilities were eliminated by effective acoustic cavity design[2].

In the context of intermediate-frequency combustion instability, a series of successful mainstage tests were conducted to measure the combustion performance of the Fastrac engine thrust chamber. The thrust chamber exhibited benign, yet marginally unstable combustion in that no damage to the thrust chamber assembly was ever sustained. A noticeble number of these tests had amplitudes of at least 10%, and most of these tests had chamber pressure oscillations with a frequency on the order of 500 Hz. This frequency was too low to be identified as acoustic or high-frequency combustion instability and too high to be identified as low-frequency combustion instability. The source of the intermediate-frequency combustion instability or "buzz" was traced to the RP-1 venturi whose violently noisy cavitation caused resonance in the feedline downstream. Combustion was stabilized by increasing the throat diameter of the fuel venturi such that the cavitation would occur more quietly. Therefore, the marginally unstable combustion was related to the facilities and not to the thrust chamber itself[3].

Now, in the context of low-frequency combustion instability, the objective was to study the characteristics of the Fastrac TCA coupled with the propellant feed system to determine if low-frequency combustion instability or "chug" could occur.

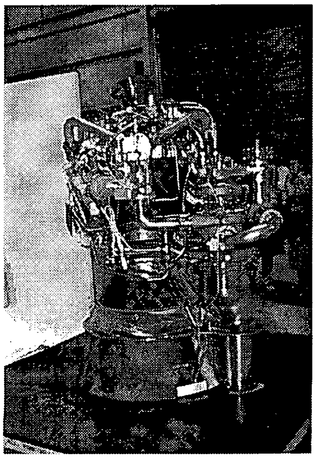

Figure-1: Fastrac Engine.

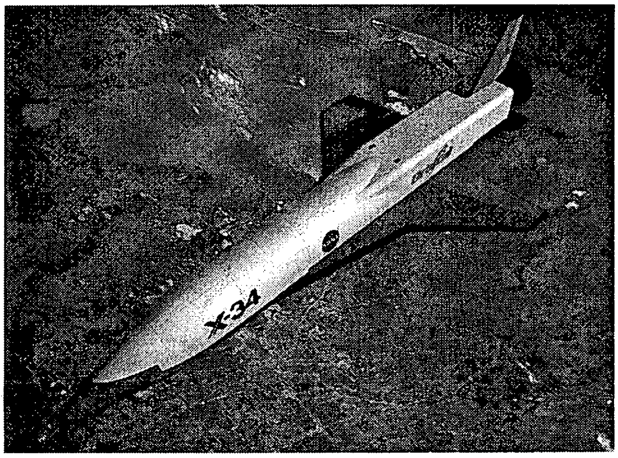

Figure-2: X-34 Vehicle.

TEST ARTICLE DESCRIPTION:

As illustrated in figures 3 and 4, the components of the Fastrac TCA test article are the thrust chamber, nozzle, fuel manifold, LOX dome, injector faceplate, and acoustic cavities. For the TCA operating conditions, the combined LOX/RP-1 flow rate is about 197 lbm/sec (89.56 Kg/sec) at a mixture ratio of 2.34. The chamber pressure is 650 psi (4.495 MPa). Details on the design of the acoustic cavities and the injector faceplate are discussed in related literature[2].

TEST FACILITY DESCRIPTION:

Testing of the Fastrac engine TCA was performed at MSFC's test stand 116. A typical test of the Fastrac engine TCA at test stand 116 is illustrated in figure-5.

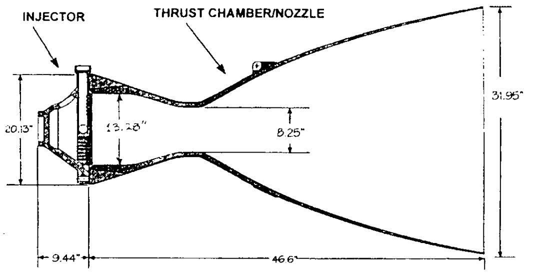

Figure-3: Fastrac Thrust Chamber Assembly.

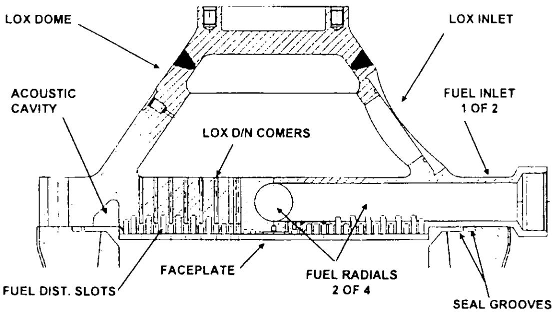

Figure-4: Fastrac Injector.

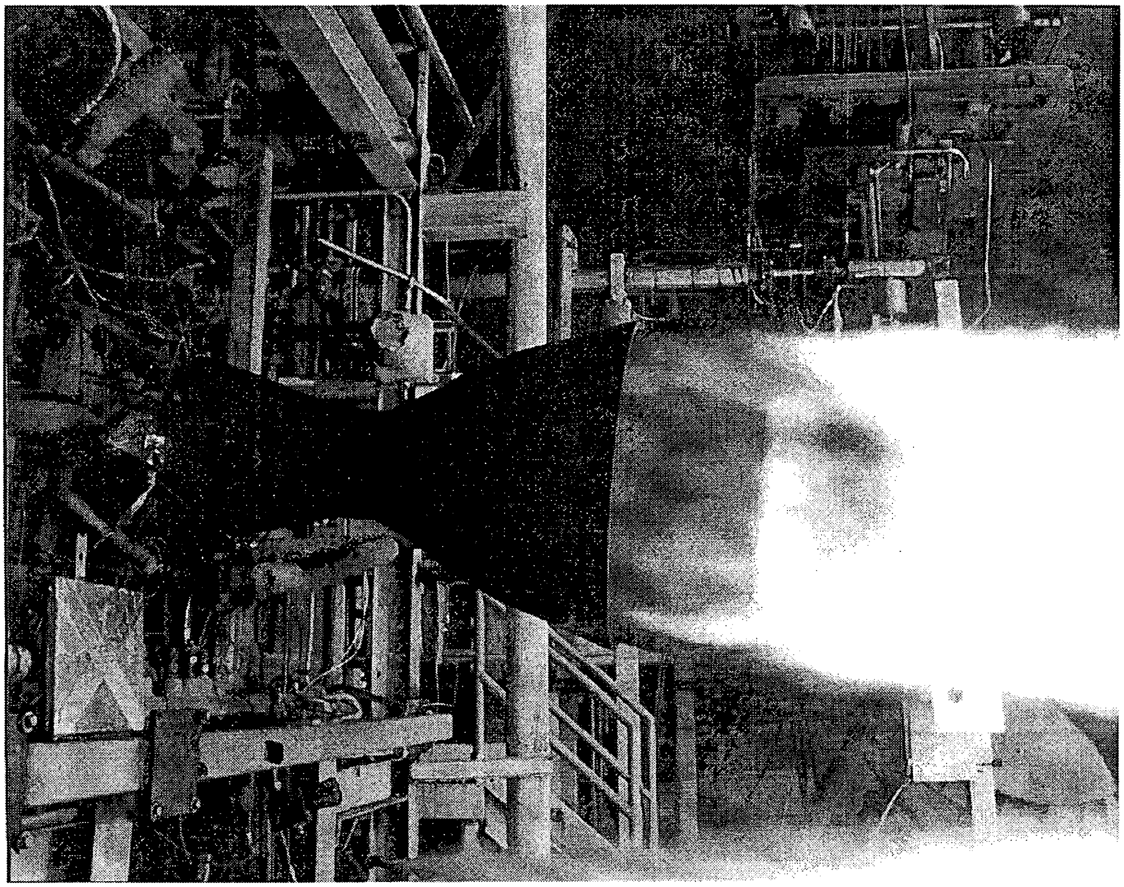

Figure-5: A typical Fastrac TCA hot-fire test at MSFC test stand 116.

The RP-1 feed system is presented in figure-6. The RP-1 feed system consisted of the RP-1 tank, the RP-1 cavitating venturi, the RP-1 valve, the RP-1 injection manifold on the TCA, and 3-inch (7.62 cm) diameter RP-1 feed lines that connect all of these components together. The RP-1 cavitating venturi had a throat diameter of 0.6121 inches (1.555 cm) and a discharge coefficient of 0.96. The RP-1 valve was about 1.792 feet (0.546 m) long. Between the RP-1 cavitating venturi and the RP-1 valve was about 11.25 feet (3.429 m) of RP-1 feed line. Between the RP-1 valve and the RP-1 injection manifold on the TCA was about 8.959 feet (2.731 m) of RP-1 feed line. Not shown in figure-6 were the “steerhorns” that started at about 6.376 feet (1.943 m) downstream of the RP-1 valve. The steerhorns was a split or bifurcation in the RP-1 feed line. The bifurcated feed lines extended about 120° apart to send RP-1 to the two inlets on opposite sides of the RP-1 injection manifold.

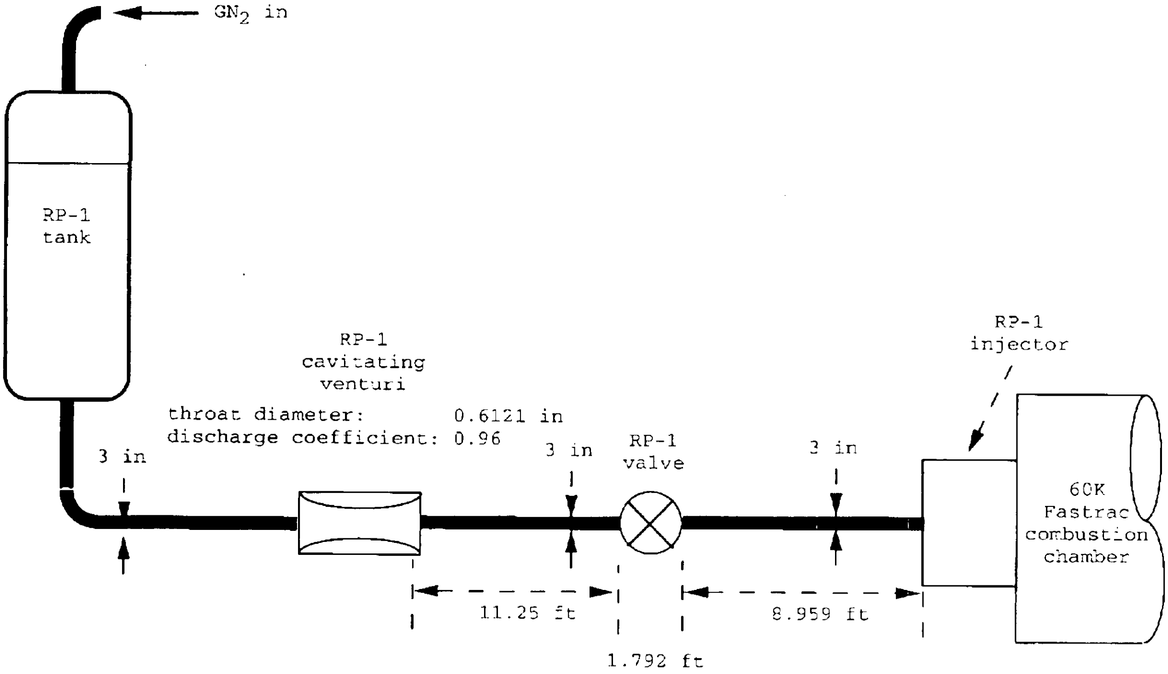

Figure-6: Test stand 116 RP-1 feed system.

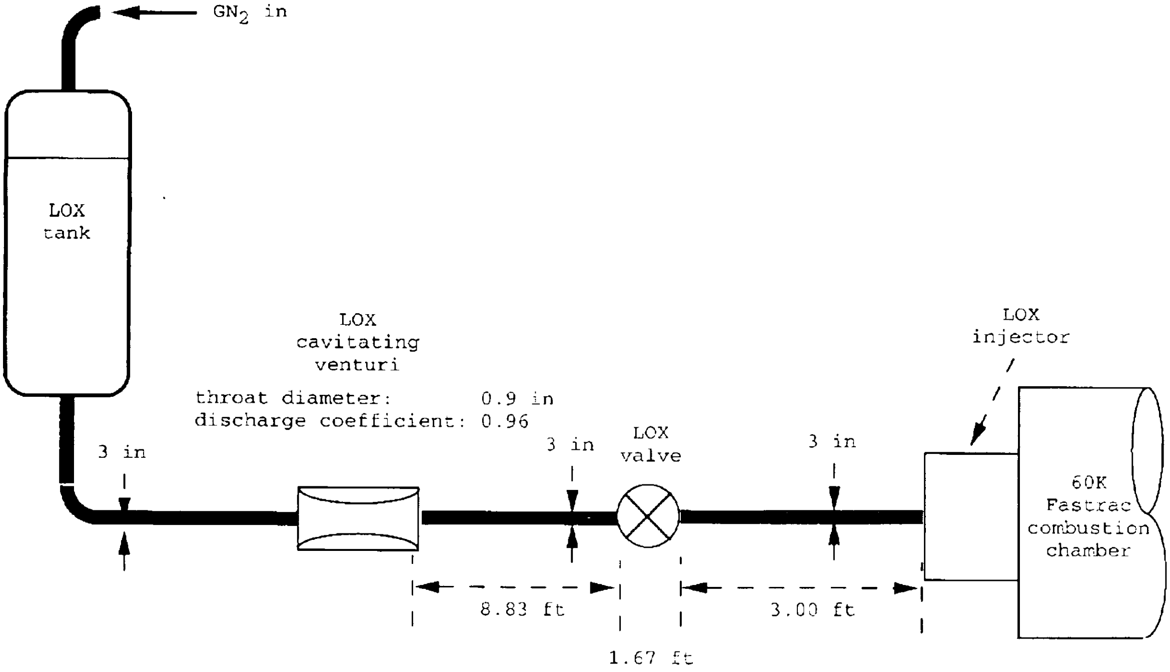

Figure-7: Test stand 116 LOX feed system.

The LOX feed system is presented in figure-7. The LOX feed system consisted of the LOX tank, the LOX cavitating venturi, the LOX valve, the LOX injection manifold on the TCA, and 3-inch (7.62 cm) diameter LOX feed lines that connect all of these components together. The LOX cavitating venturi had a throat diameter of 0.9 inches (2.286 cm) and a discharge coefficient of 0.96. The LOX valve was about 1.67 feet (0.509 m) long. Between the LOX cavitating venturi and the LOX valve was about 8.83 feet (2.691 m) of LOX feed line. Between the LOX valve and the LOX injection manifold on the TCA was about 3 feet (0.914 m) of LOX feed line.

TEST PROCEDURE:

A typical mainstage test was initiated by slightly opening the LOX valve to allow a small amount of LOX flow to chill the LOX feedline downstream and LOX injector prior to ignition. During pre-chill, this small amount of LOX flow vaporized upon injection into the chamber and was discharged out through the nozzle. Ignition was performed by injecting TEA/TEB into the chamber while maintaining this small amount of LOX flow. After ignition, fuel-rich "level-1" combustion was initiated by completely opening the RP-1 valve to allow the full amount of RP-1 flow to be injected into the chamber. Simultaneously, the TEA/TEB flow was terminated and the small amount of LOX flow was maintained. After level-1 combustion was briefly established, oxidizer-rich "level-2" combustion was initiated by completely opening the LOX valve to allow the full amount of LOX flow to be injected into the chamber. Level-2 combustion constituted mainstage operation of the Fastrac TCA.

Chamber pressures for level-1 and level-2 combustion were 450 psi (3.06 MPa) and 650 psi (4.42 MPa), respectively.

Those feed systems inactive during pre-chill, ignition, level-1, and level-2 operations were purge with nitrogen gas to prevent backflow into the injector.

Table-1: Fastrac TCA Mainstage Test Results

Test #	Type	Duration (sec)	Frequency (Hz)	Pc (psi/MPa)	δPc/Pc (%)
1	ignition	n/a	n/a	n/a	n/a
2	ignition	n/a	n/a	n/a	n/a
3	level-1	5	410	450/3.06	11.8
4	level-2	7	513	644/4.38	5.1
5	level-2	25	508	625/4.25	11.1
6	not successful	n/a	n/a	n/a	n/a
7	level-2	25	522	643/4.37	8.1
8	level-2	53	522	650/4.42	10.2
16	level-2	8	527	641/4.36	9.2
17	level-2	27	527	631/4.29	10.5
19	level-2	130	522	640/4.35	11.9
20	level-2	17	508	645/4.39	8.5
21	level-2	17	503	641/4.36	8.9
22	level-2	17	493	635/4.32	12.9
23	level-2	150	498*	656/4.46	3.0
24	level-2	150	515*	664/4.52	3.9
25	level-2	6	142	649/4.41	6.8
26	level-2	150	*	664/4.52	2.9

SUMMARY OF MAINSTAGE TESTS:

The results of the mainstage tests are presented in table-1. The amplitudes presented were determined by visual averaging and are not RMS values, which will be lower. Out of the 15 successful mainstage tests, 10 of these tests had amplitudes of at least 8%, and 6 of these tests had amplitudes of at least 10%. These noticebly large-amplitudes in chamber pressure were mostly associated with the 500 Hz intermediate-frequency combustion instability or buzz.

Tests 1 and 2 were ignition tests. Test-3 was a level-1 test that exhibited large amplitude chamber pressure oscillations at 410 Hz. Test-6 was unsuccessful. Tests 9-15, and 18 were not included in table-1 since these were bomb-tests[2]. Tests 16, 17, and 19 were level-2 tests conducted to obtain acoustic cavity temperatures. Tests 23 and 24 were level-2 tests that not only had the 500 Hz oscillation, but had oscillations at 60 Hz and its harmonics indicated by the asterisk in the frequency column.Test-25 was the first level-2 test where the 500 Hz oscillation was eliminated, leaving behind what could be interpreted as low-amplitude chug. Test-26 was the second level-2 test where the 500 Hz oscillation was eliminated leaving only low-amplitude oscillations at 60 Hz and its harmonics indicated by the asterisk in the frequency column. Tests 27-31 also were not included in table-1 since these were additional bomb tests.

CHARACTERIZATION OF CHAMBER PRESSURE OSCILLATIONS:

Presented in table-2 are the natural frequencies of the combustion chamber acoustic modes. These frequencies were based on a chamber diameter of 13.28 inches (33.73 cm) and a chamber speed of sound of 3628.8 ft/sec (1106.1 m/sec). The frequencies of chamber pressure oscillations of interest were too low to be high-frequency. Also, the frequencies of chamber pressure oscillations of interest were lower than the 500 Hz buzz that was traced to the fuel venturi. Therefore, the frequency of the chamber pressure oscillations of interest were too low to be considered intermediate-frequency. Therefore, the chamber pressure oscillations of interest were low-frequency.

Table-2: Fastrac TCA Chamber Acoustic Frequencies

Tangential modes		Radial modes		Mixed modes	
1T	1922 Hz	1R	4000 Hz	1T-1R	5565 Hz
2T	3188 Hz	2R	7322 Hz	1T-2R	8900 Hz
3T	4385 Hz	3R	10,618 Hz	2T-1R	7000 Hz
4T	5550 Hz				

REVIEW OF MODEL IMPLEMENTATION FOR THE PRESSURE-FED FASTRAC TCA:

To perform qualitative predictions of low-frequency combustion instability, a linear model was formulated. The formulation of this model was based on the model of Wenzel and Szuch[4] with two very important improvements. The first improvement was the modeling of each of the propellant feed systems extending from the injectors up to the venturis. The second improvement was the assumption of a non-zero damping coefficient. Therefore, not only was it possible to generate a neutral stability boundary for a damping coefficient of zero, it was also possible to determine the frequency and damp time for chamber pressure oscillations given the steady-state chamber pressure and steady-state injector pressure drops. The details on the formulation are lengthly and will not be discussed here, but in the appendix.

The model was implemented by first specifying the parameters of the Fastrac TCA combustion chamber, the oxidizer feed system, and the fuel feed system, all at test stand 116 during test-8.

For the combustion chamber, the volume from the injector faceplate down to the throat was determined from the formula of characteristic length[5]:

$$L^{*} = \frac{V_C}{A_T} = L_{CY}\varepsilon_C + \frac{L_{CO}}{3}\left(\varepsilon_C + \sqrt{\varepsilon_C} + 1\right) . \tag{1}$$

Where A_T is the throat cross-sectional area, L_{CY} is the combustion chamber length from the injector face to the nozzle inlet, L_{CO} is the nozzle length from the inlet to the throat, and ε_C is the chamber contraction ratio. The from figure-3, Fastrac TCA combustion chamber was 13.28 inches (33.73 cm) diameter at the injector face, and 8.25 inches (20.96 cm) diameter at the throat. This gave a contraction ratio and a throat cross-sectional area of 2.59 and 53.45616 in^2 (344.88 cm^2), respectively. Additionally, the distance from the injector face to the nozzle inlet was 2.7 inches (6.86 cm), and the distance from the nozzle inlet to the throat was 15.3 inches (38.86 cm). Substituting these values into equation-1 gave a characteristic length of 33.52018 inches (85.14 cm). Multiplying the characteristic length and the throat cross-sectional area gave a chamber volume of $V_C = 1.03696$ ft^3 (0.02936 m^3).

For a chamber pressure of 650 psi (4.422 MPa) and a mixture ratio of 2.34, a thermochemical equilibrium calculation determined that the temperature and density of the combustion products was $T_C = 6397°R$ (3550°K) and $\rho_C = 0.212$ lbm/ft^3 (3.403 kg/m^3), respectively. Since the total flow rate was 197 lbm/sec (89.55 kg/sec) and the combustion chamber flush/fill time was defined as:

$$\tau_C = \frac{\rho V_C}{\bar{\dot{m}}} \quad . \tag{2}$$

The combustion chamber flush/fill time was $\tau_C = 1.11592 \times 10^{-3}$ seconds. Also, at a chamber pressure of 650 psi and a mixture ratio of 2.34, a thermochemical equilibrium calculation determined that the derivative of the chamber gas temperature with respect to the mixture ratio was -228.29°R (-126.67°K). The test-8 chamber pressure was 658 psi (4.476 MPa).

The cross-sectional areas of the opened LOX valve and the LOX dome inlet were 7.06858 in^2 (45.60 cm^2) and 4.53144 in^2 (29.24 cm^2), respectively. These were based on local feedline diameters of 3.0 inches (7.62 cm) and 2.402 in (6.10 cm), respectively. However, the total cross-sectional area of all of the LOX orifices was 3.04797 in^2 (19.66 cm^2). The lengths of the LOX valve, the LOX dome inlet and the faceplate thickness for the LOX orifices were 20 in (50.80 cm), 6 in (15.24 cm) (assumed), and 0.24250 in (5.08 cm).

The volumes of the LOX feed system segments were 748.98710 in^3 (12,273.70 cm^3), 163.13171 in^3 (2673.25 cm^3), and 287.41303 in^3 (4709.86 cm^3) for the LOX feedline upstream of the valve, the LOX feedline upstream of the injector inlet, and the LOX dome, respectively.

The LOX feed system pressures were 1088.1 psi (7.402 MPa), 936.3 psi (6.369 MPa), and 784.5 psi (5.337 MPa), upstream of the LOX valve, upstream of the LOX dome inlet, and in the LOX dome, respectively. All of the LOX feed system pressures were obtained from test-8.

The LOX flow rate was 138 lbm/sec (62.73 kg/sec) and the time lag required for 50% of the LOX droplet mass to evaporate was previously determined to be 3.00775×10^{-2} seconds[6].

The cross-sectional areas of the opened RP-1 valve and the RP-1 injector manifold inlet were 5.49467 ft^2 and 5.49292 ft^2, respectively. These were based on feedline diameter of 2.645 in (6.72 cm) upstream of the "steerhorn" bifurcation and 1.870 in (4.75 cm) downstream of the steerhorn bifurcation, respectively. However, the total cross-sectional area of all of the RP-1 orifices was 1.35362 in^2 (8.73 cm^2). The lengths of the RP-1 valve, the RP-1 injector manifold inlet and the faceplate thickness for the RP-1 orifices were 21.50400 in (54.62 cm), 6 in (15.24 cm) (assumed), and 0.24250 in (0.62 cm).

The volumes of the RP-1 feed system segments were 954.25877 in^3 (15,637.50 cm^3), 590.66630 in^3 (9679.29 cm^3), and 89.70048 in^3 (1469.93 cm^3) for the RP-1 feedline upstream of the valve, the RP-1 feedline upstream of the injector inlet, and the RP-1 injector manifold, respectively.

Note that the cross-sectional area of the RP-1 injector manifold inlet and the volume of the RP-1 feedlines upstream of the RP-1 injector manifold reflect the actual bifurcated "steerhorns" configuration of feedlines not illustrated in figure-6.

The RP-1 feed system pressures were 832.30 psi (5.662 MPa), 810.25 psi (5.512 MPa), and 788.20 psi (5.362 MPa), upstream of the RP-1 valve, upstream of the RP-1 injector inlet, and in the RP-1 injector manifold, respectively. All of the RP-1 feed system pressures were obtained from test-8.

The RP-1 flow rate was 59 lbm/sec (26.82 kg/sec) and the time lag required for 50% of the LOX droplet mass to evaporate was previously determined to be 3.58088×10^{-2} seconds[6].

The low-frequency combustion stability map for the Fastrac TCA with the pressure-fed propellant feed system is presented in figure-8. The test-8 RP-1 injector pressure drop was 0.19787. The test-8 LOX injector pressure drop was 0.19225.

To generate a curve on the low-frequency combustion stability map, first a frequency bandwidth was selected. In figure-8, a typical bandwidth coresponding to zero growth rate was from 67 Hz to 103 Hz. Secondly, a pressure oscillation growth rate was selected. A positive growth rate indicated unstable oscillations in pressure. A negative growth rate indicated stable oscillations in pressure. A zero growth rate indicated neutrally stable oscillations in pressure. The growth rate was arbitrarily varied from –75/sec to 75/sec.

According to equation-129, solving for the RP-1 injector pressure drop required solving a quadratic equation. Since equation-129 was solved by implementing the quadratic formula in equation-130, both "positive" and "negative" solutions for the RP-1 injector pressure drop were searched for the actual solution. Then, equation-128 was used to determined the LOX injector pressure drop from the RP-1 injector pressure drop. By trial and error, a growth rate was selected until the curve passed through the injector operating point. Therefore, the growth rate of the amplitude and the frequency of pressure oscillations were determined in this manner. Therefore, in figure-8, the frequency and growth rate of pressure oscillations in test-8 of the Fastrac TCA, tested at test stand 116 were 64.93 Hz and –68.5/sec (stable), respectively.

Interpreting the frequency was straight forward. However, interpreting the growth rate was not as trivial. If one assumed that the damp time was the amount of time required by the pressure oscillation to damp down to 50% of its original amplitude, then:

$$t_{\mathrm{DAMP}} = -\frac{(0.69315)}{\lambda} . \tag{3}$$

Therefore, with a growth rate of –68.5/seconds, a pressure oscillation of 64.93 Hz would damp to 50% of its initial amplitude in 10.12 milliseconds. In other words, a mainstage pressure oscillation with a frequency of 64.93 Hz and an initial amplitude of 20% of the mean chamber pressure would damp to an amplitude of 10% of the mean chamber pressure after 10.12 milliseconds. This damp time was extremely short if one considered that for the maximum damp time[1], given by:

$$t_{\mathrm{MAX\ DAMP}} = \frac{\left(1250\ \mathrm{msec} - \mathrm{Hz}^{1/2}\right)}{\sqrt{\omega}} , \tag{4}$$

gave 155.13 milliseconds.

Also, in figure-8, it was apparent that the first fictitious operating point $\Delta P_F/P_C = 0.200$ and $\Delta P_O/P_C = 0.126$ was an intersection of several curves. This was a situation where a single combination of $\Delta P_F/P_C$ and $\Delta P_O/P_C$ gave several combinations of frequencies and growth rates. Recall that a single frequency and growth rate represents a damped (for negative growth rate), sinusoidal function, which was a solution of a set of ordinary differential equations. Since there were no initial conditions given, all possible solutions will stand ambiguously. The only certainty for such a point is that since the growth rates for all three curves were negative, then the pressure oscillations would be stable regardless of the frequency.

Additionally, in figure-8, it was apparent that the second fictitious operating point $\Delta P_F/P_C$ = 4.500 and $\Delta P_O/P_C$ = 0.060 was an intersection of a couple of curves. This was a situation where a single combination of $\Delta P_F/P_C$ and $\Delta P_O/P_C$ gave two combinations of frequencies and growth rates. Again, recall that a single frequency and growth rate represents a damped (for negative growth rate), sinusoidal function, which was a solution of a set of ordinary differential equations. Since there were no initial conditions given, all possible solutions will stand ambiguously. Unlike the first fictitious operating point, the stability would be less certain since one curve had a positive growth rate and the other curve had a negative growth rate. Although this operating point was more likely to be unstable, it would not be a realistic operating point due to the extremely high RP-1 injector pressure drop.

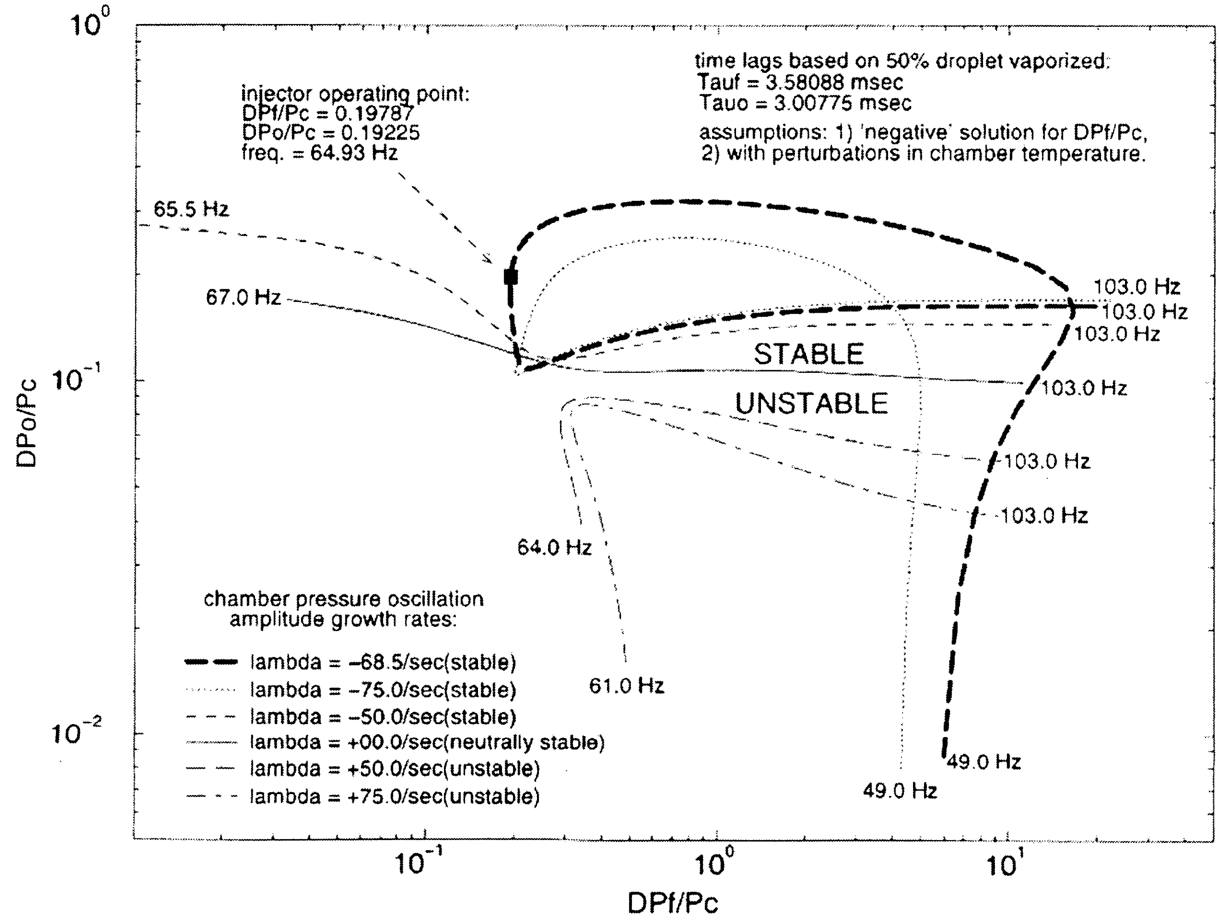

Figure-8: low-frequency combustion stability map for test-8 of the pressure-fed Fastrac engine TCA tested at MSFC test stand 116.

REVIEW OF MODEL IMPLEMENTATION FOR THE PUMP-FED FASTRAC TCA:

The model was again implemented by first specifying the parameters of the Fastrac TCA combustion chamber, the pump-fed oxidizer feed system, and the pump-fed fuel feed system, all integrated together as a flight engine, tested at SSC.

For the combustion chamber, the geometry, the chamber pressure, the mixture ratio, and the total flow rate are all unchanged in the conversion from a pressure-fed to a pump-fed propellant feed system. The only changes are in the LOX and RP-1 feed systems. These changes in the LOX and RP-1 feed systems were reflected in the line length and line diameter measurements in figures 9 and 10, repectively. Unfortunately, the venturis were not replaced by a pumps as a flow rate-setting device.

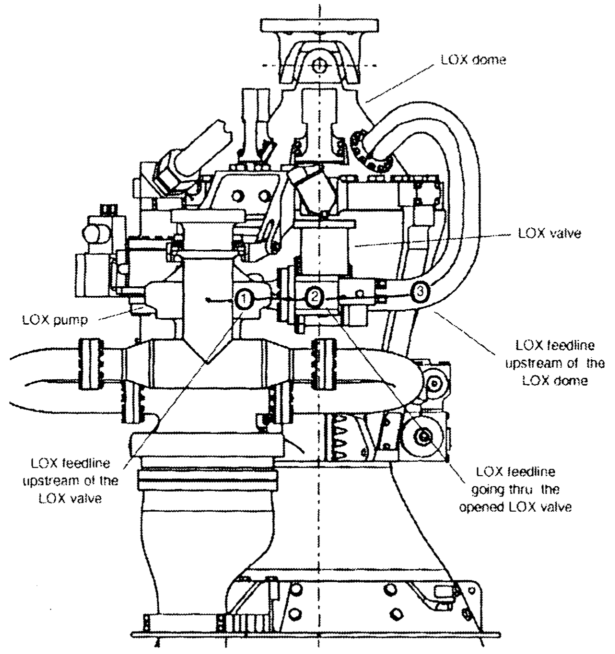

Figure-9: LOX feedline segments on the upper portion of the Fastrac flight engine (front view).

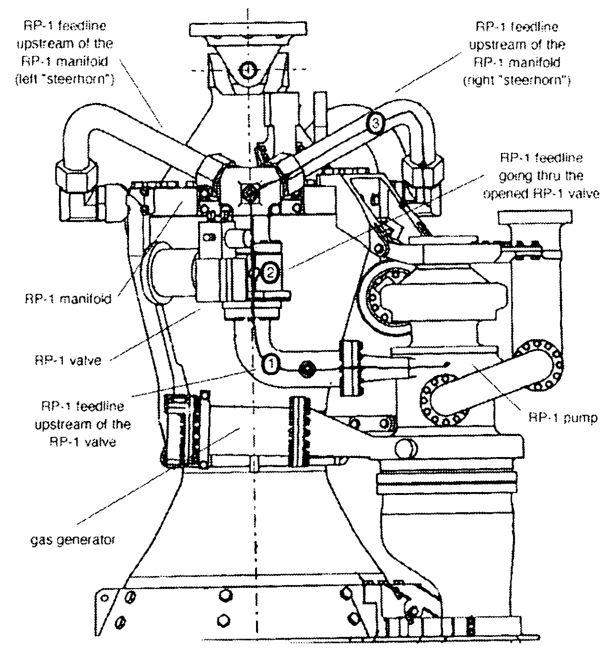

Figure-10: RP-1 feedline segments on the upper portion of the Fastrac flight engine (left view).

Referring to figure-9, the lengths and diameters along the LOX feedline are:

$$L_1 = 6.50 \text{ in } (16.51 \text{ cm}),\ D_1 = 2.645 \text{ in } (6.72 \text{ cm})$$

$$L_2 = 4.33 \text{ in } (11.00 \text{ cm}),\ D_2 = 2.645 \text{ in } (6.72 \text{ cm})$$

$$L_3 = 31.9 \text{ in } (81.03 \text{ cm}),\ D_3 = 2.402 \text{ in } (6.10 \text{ cm})$$

Referring to figure-10, the lengths and diameters along the RP-1 feedline are:

$$L_1 = 19.51 \text{ in } (49.56 \text{ cm}),\ D_1 = 2.635 \text{ in } (6.69 \text{ cm})$$

$$L_2 = 4.33 \text{ in } (11.00 \text{ cm}),\ D_2 = 2.645 \text{ in } (6.62 \text{ cm})$$

$$L_3 = 27.46 \text{ in } (69.75 \text{ cm}),\ D_3 = 1.870 \text{ in } (4.75 \text{ cm})$$

The cross-sectional areas of the opened LOX valve and the LOX dome inlet were unchanged at 5.49467 in^2 (35.45 cm^2) and 4.53144 in^2 (29.24 cm^2), respectively. These were based on local feedline diameters of 2.645 inches and 2.402 in, respectively. However, the total cross-sectional area of all of the LOX orifices was 3.04797 in^2 (19.66 cm^2). The lengths of the LOX valve, the LOX dome inlet and the faceplate thickness for the LOX orifices were 4.33 in (11.00 cm), 6 in (15.24 cm) (assumed), and 0.24250 in (0.62 cm).

The volumes of the LOX feed system segments were 35.71532 in^3 (585.27 cm^3), 144.55282 in^3 (2368.80 cm^3), and 287.41303 in^3 (4709.86 cm^3) for the LOX feedline upstream of the valve, the LOX feedline upstream of the injector inlet, and the LOX dome, respectively. While the LOX dome volume was unchanged, the volumes of the LOX feedlines upstream of the valve and upstream of the LOX injector inlet were reduced to reflect the shortening of the LOX feedlines.

The LOX feed system pressures were unchanged at 1088.1 psi (7.402 MPa), 936.3 psi (6.369 MPa), and 784.5 psi (5.337 MPa), upstream of the LOX valve, upstream of the LOX dome inlet, and in the LOX dome, respectively. All of the LOX feed system pressures were obtained from test-8.

The LOX flow rate was unchanged at 138 lbm/sec (62.73 kg/sec) and the time lag required for 50% of the LOX droplet mass to evaporate was also unchanged at 3.00775 x 10^{-2} seconds.

The cross-sectional areas of the opened RP-1 valve and the RP-1 injector manifold inlet were unchanged at 5.49467 ft^2 (0.51047 m^2) and 5.49292 ft^2 (0.51031 m^2), respectively. These were based on feedline diameter of 2.645 in upstream of the "steerhorn" bifurcation and 1.870 in downstream of the steerhorn bifurcation, respectively. However, the total cross-sectional area of all of the RP-1 orifices was 1.35362 in^2. The lengths of the RP-1 valve, the RP-1 injector manifold inlet and the faceplate thickness for the RP-1 orifices were 4.33 in (11.00 cm), 5.36 in (13.61 cm), and 0.24250 in (0.62 cm).

The volumes of the RP-1 feed system segments were changed to 106.39186 in^3 (1743.45 cm^3), 178.14401 in^3 (2919.26 cm^3), and 89.70048 in^3 (1469.93 cm^3) for the RP-1 feedline upstream of the valve, the RP-1 feedline upstream of the injector inlet, and the RP-1 injector manifold, respectively.

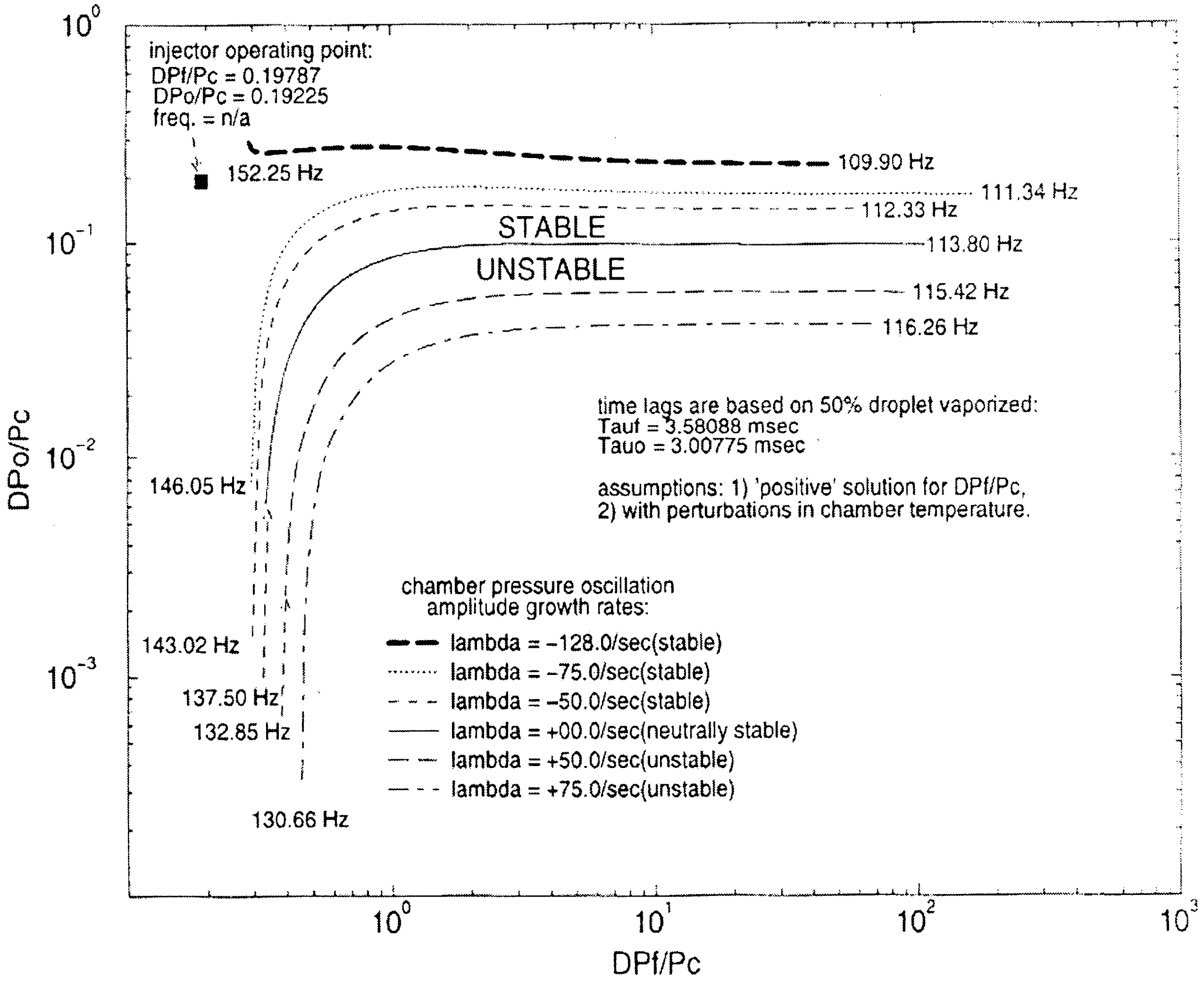

Figure-11: low-frequency combustion stability map for the pump-fed Fastrac engine TCA tested at SSC.

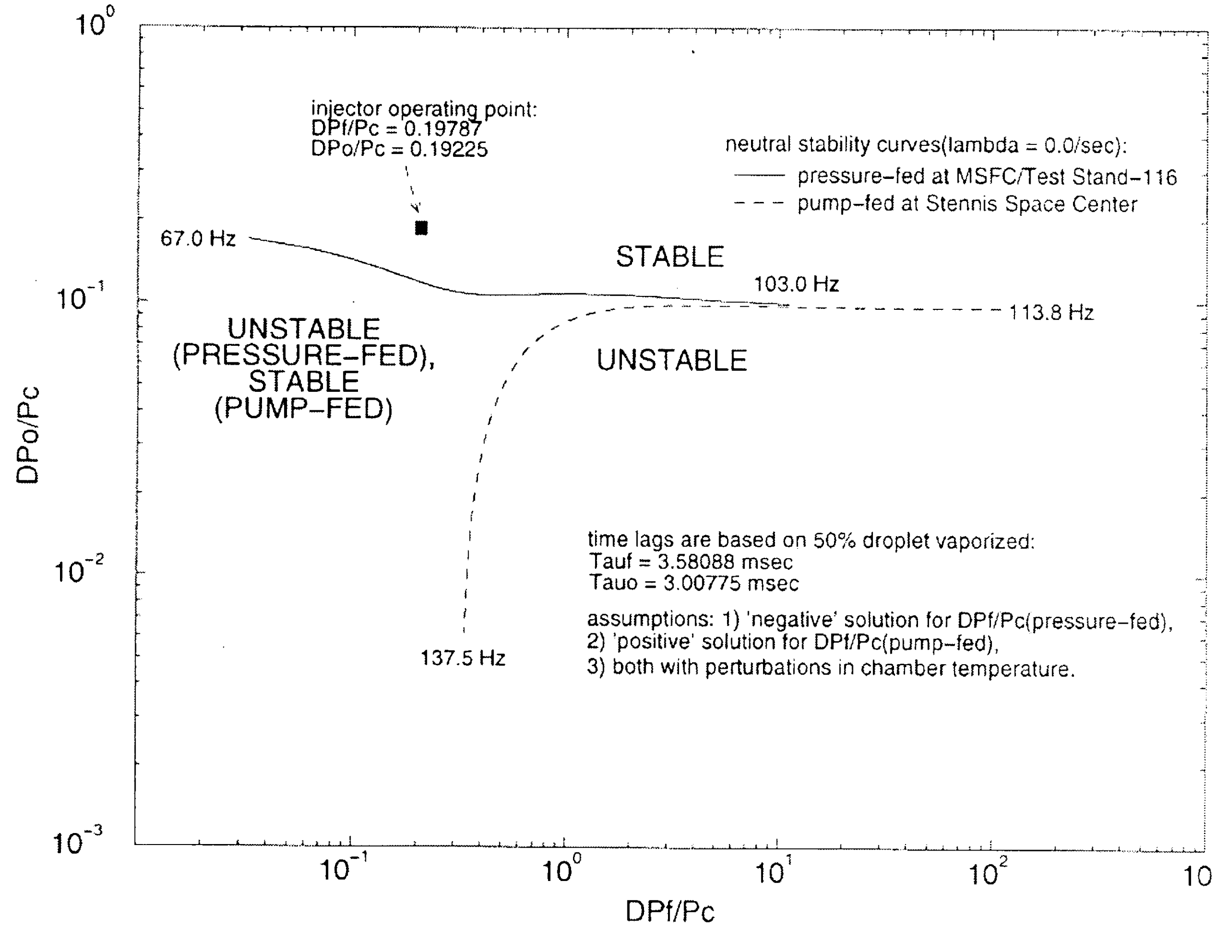

Figure-12: low-frequency combustion stability map for the pressure-fed Fastrac engine TCA tested at MSFC and the pump-fed Fastrac engine TCA tested at SSC.

As in the case of the pressure-fed TCA, note that the cross-sectional area of the RP-1 injector manifold inlet and the volume of the RP-1 feedlines upstream of the RP-1 injector manifold reflect the actual bifurcated "steerhorns" configuration of feedlines not illustrated in figure-6.

The RP-1 feed system pressures were 832.30 psi (5.662 MPa), 810.25 psi (5.512 MPa), and 788.20 psi (5.362 MPa), upstream of the RP-1 valve, upstream of the RP-1 dome inlet, and in the RP-1 injector manifold, respectively. All of the RP-1 feed system pressures were obtained from test-8.

The RP-1 flow rate was unchanged at 59 lbm/sec (26.82 kg/sec) and the time lag required for 50% of the LOX droplet mass to evaporate was 3.58088 x 10^{-2} seconds.

The low-frequency combustion stability map for the Fastrac TCA with the pump-fed propellant feed system is presented in figure-11. The LOX and RP-1 injector pressure drops for the SSC flight engine were assumed to be the same as the test-8 LOX and RP-1 injector pressure drops, which was 0.19225 and 0.19787, respectively. A typical frequency bandwidth corresponding the zero growth rate was from 113.8 Hz to 137.5 Hz. Frequency decreased as $\Delta P_F/P_C$ increased. This was the exact opposite of figure-8, where frequency increased as $\Delta P_F/P_C$ increased. As in figure-8, a pressure oscillation growth rate was selected. A positive growth rate indicated unstable oscillations in pressure. A negative growth rate indicated stable oscillations in pressure. A zero growth rate indicated neutrally stable oscillations in pressure. The growth rate was arbitrarily varied from −75/sec to 75/sec. Along the neutral stability curve, $\Delta P_O/P_C$ seemed to be constant with $\Delta P_F/P_C$ until $\Delta P_F/P_C$

was about 100%, Below a $\Delta P_F/P_C$ of 100%, $\Delta P_O/P_C$ decreased rapidly with decreasing $\Delta P_O/P_C$. Likewise, the curves corresponding to positive growth rate and negative growth rate followed the trends of the neutral stability curve as they ran below and above it, respectively. Despite all trial-n-error attempts to choose a negative growth rate such that would produce a curve that would run through the injector operating point, none could be found. The best curve that could be produced corresponded to a growth rate of –128/sec. Therefore, the negative growth rate and the frequency of pressure oscillations corresponding to the injector operating point could not be determined. All that could be said about this point was that the pressure oscillations were likely to be qualitatively stable.

In figure-12, the neutral stability curves for the pressure-fed and the pump-fed Fastrac TCA are compared. The curve for the pressure-fed TCA was obtained from the "negative" solution of equation-130. The curve for the pump-fed TCA was obtained from the "positive" solution of equation-130. For the curve corresponding to the pressure-fed TCA, the frequency increased as $\Delta P_F/P_C$ increased. However, for the curve corresponding to the pump-fed TCA, the frequency decreased with increasing $\Delta P_F/P_C$. By comparing the behavior of the neutral stability curves, one can conclude that for extremely high valves of $\Delta P_F/P_C$, shortening the propellant feedlines to convert from a pressure-fed system to a pump-fed system will make no difference in the low-frequency combustion stability of the TCA. However, one can conclude that for realistically low values of $\Delta P_F/P_C$, shortening the propellant feedlines to convert from a pressure-fed system to a pump-fed system will make a dramatic increase in the low-frequency combustion stability of the TCA.

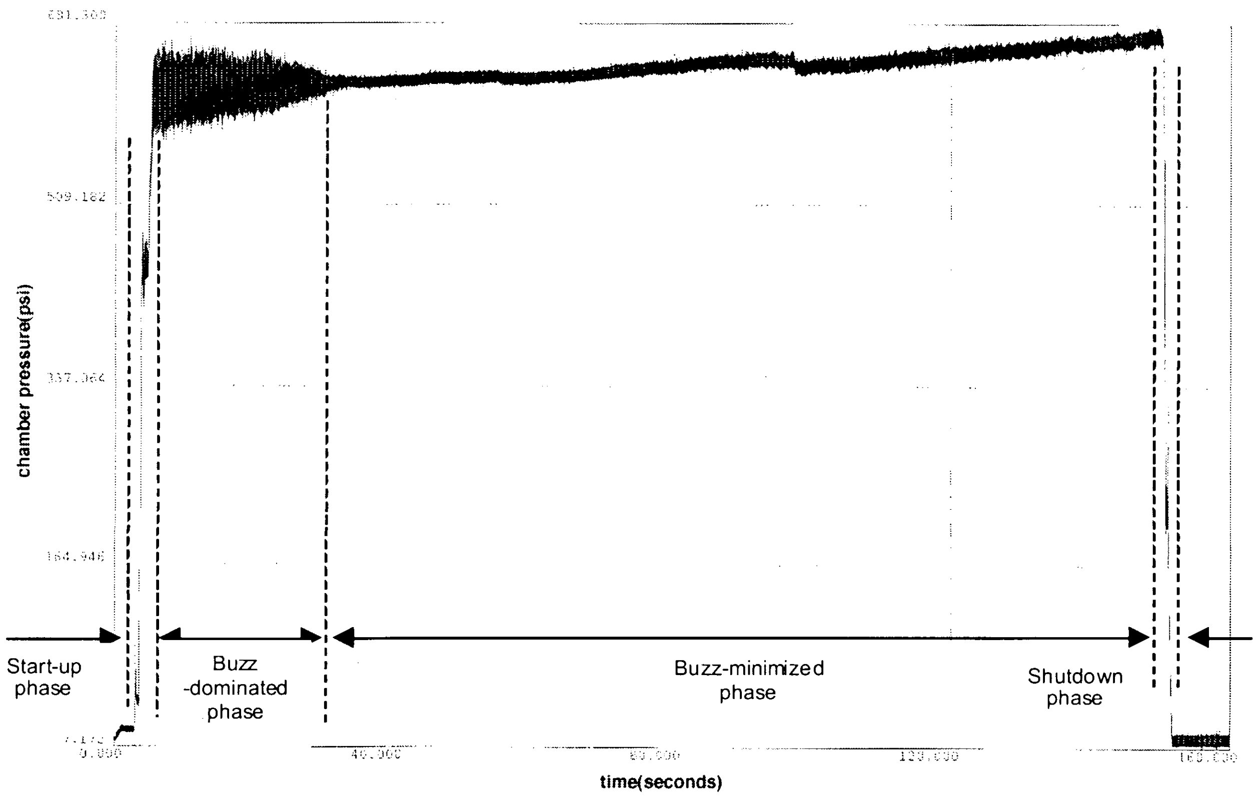

Figure-13: test-23 chamber pressure.

REVIEW OF TEST DATA

In figure-13, the test-23 chamber pressure is presented as a function of time. This chamber pressure vs. time data is also typical of tests 24, 25, and 26. With the exception of test-25, these tests were 150 seconds in duration. In these tests the chamber pressure data was divided into four phases. The first phase was start-up. The second phase was buzz-dominated mainstage. The third phase is buzz-minimized or buzz-free mainstage. The fourth stage is shutdown. Tests 23 and 24 had all four phases. However, tests 25 and 26 had only three phases since there was no buzz-dominated mainstage.

In figure-14, the test-23 chamber pressure during the start-up phase is presented. In figure-14, the TCA is powering-up from ignition to level-1 operation. As it did so, chug was exhibited with an amplitude of 10.3% of steady-state chamber pressure, with a spectral intensity of 14.424 psi/Hz (98.122 KPa/Hz) at a frequency of 195 Hz. The duration of this chug was about 139 milliseconds.

In figure-15, the test-23 chamber pressure during the buzz-dominated phase is presented. In figure-15, the TCA was operating at level-2 conditions. As it did so, buzz dominated the spectrum with an intensity of 8.295 psi/Hz (56.429 KPa/Hz) at a frequency of 493 Hz. The buzz decayed away by about 35 seconds. In addition to the buzz, some low-intensity, low-frequency peaks in the spectrum appeared with a magnitude of 1.794 psi/Hz (12.204 KPa/Hz) at 59 Hz, 2.406 psi/Hz (16.367 KPa/Hz) at 127 Hz, 3.0 psi/Hz (20.408 KPa/Hz) at 195 Hz, and 1.505 psi/Hz (10.238 KPa/Hz) at 269 Hz. The duration of the buzz during this phase was about 30 seconds. The maximum amplitude was about 7.6% of the steady-state chamber pressure.

In figure-16, the test-23 chamber pressure during the buzz-minimized phase is presented. In figure-16, the TCA was still operating at level-2 conditions. As it did so, the intermediate-frequency oscillation appeared in the spectrum with a lower intensity of 1.147 psi/Hz (7.803 KPa/Hz) at a frequency of 498Hz. Additionally, some low-frequency oscillations appeared in the spectrum with a magnitude of 1.958 psi/Hz (13.320 KPa/Hz) at 59 Hz, 1.742 psi/Hz (11.850 KPa/Hz) at 181 Hz, 0.490 psi/Hz (3.333 KPa/Hz) at 269 Hz, and 0.502 psi/Hz (3.415 KPa/Hz) at 298 Hz. The duration of this phase was about 114 seconds. The average amplitude was about 2.4% of the steady-state chamber pressure.

The test-23 chamber pressure during the shut-down phase is presented. The TCA was powering-down from level-2 operation. As it did so, chug was exhibited in several sub-phases. The first and third sub-phases are presented in figures-17 and 18, respectively. In the first shut-down sub-phase, chug was exhibited with an amplitude of about 9.6% of steady-state chamber pressure, with a spectral intensity of 10.802 psi/Hz (73.483 KPa/Hz) at a frequency of 68 Hz, 3.831 psi/Hz (26.061 KPa/Hz) at 132 Hz , and 3.828 psi/Hz (26.041 KPa/Hz) at 142 Hz. The duration of chug in the first shut-down sub-phase was 425 milliseconds. In the third shut-down sub-phase, chug was exhibited with an amplitude of about 18.4% of steady-state chamber pressure, with a spectral intensity of 14.320 psi/Hz (97.415 KPa/Hz) at a frequency of 156 Hz. The duration of chug in the third shut-down sub-phase was 201 milliseconds. There was not a second shut-down sub-phase for test-23.

Consider the test-24 chamber pressure during the start-up phase. Chug was exhibited with an amplitude of about 32.8% of steady-state chamber pressure, with a spectral intensity of 30.436 psi/Hz (207.048 KPa/Hz) at a frequency of 195 Hz. The duration of this chug was about 185 milliseconds.

Consider the test-24 chamber pressure during the buzz-dominated phase. As the TCA was operating at level-2 conditions, buzz dominated the spectrum with an intensity of 13.635 psi/Hz (92.755 KPa/Hz) at a frequency of 498 Hz. The buzz decayed away by about 54 seconds. In addition to the buzz, some low-intensity, low-frequency peaks in the spectrum appeared with a magnitude of 2.259 psi/Hz (15.367 KPa/Hz) at 59 Hz, 5.983 psi/Hz (40.701 KPa/Hz) at 132 Hz, and 3.211 psi/Hz (21.844 KPa/Hz) at 195 Hz. The duration of the buzz during this phase was about 48.5 seconds. The maximum amplitude was about 13.3% of the steady-state chamber pressure.

Consider the test-24 chamber pressure during the buzz-minimized phase. As the TCA was still operating at level-2 conditions, the intermediate-frequency oscillation appeared in the spectrum with a lower intensity of 2.130 psi/Hz (14.490 KPa/Hz) at a frequency of 503 Hz. Additionally, some low-frequency oscillations appeared in the spectrum with a magnitude of 1.749 psi/Hz (11.898 KPa/Hz) at 59 Hz, 1.683 psi/Hz (11.449 KPa/Hz) at 181 Hz, 0.369 psi/Hz (2.510 KPa/Hz) at 273 Hz, and 0.512 psi/Hz (3.483 KPa/Hz) at 298 Hz. The duration of this phase was about 98 seconds. The average amplitude was about 2.3% of the steady-state chamber pressure.

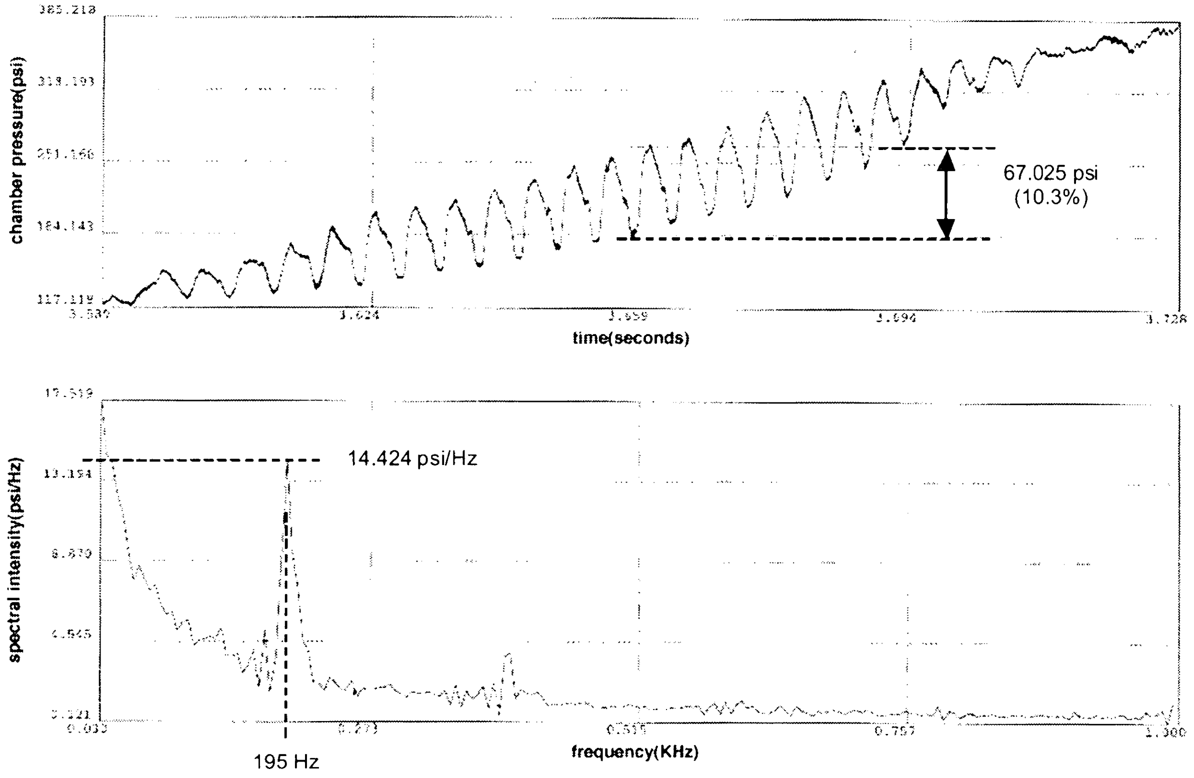

Figure-14: test-23 chamber pressure chug during the start-up phase.

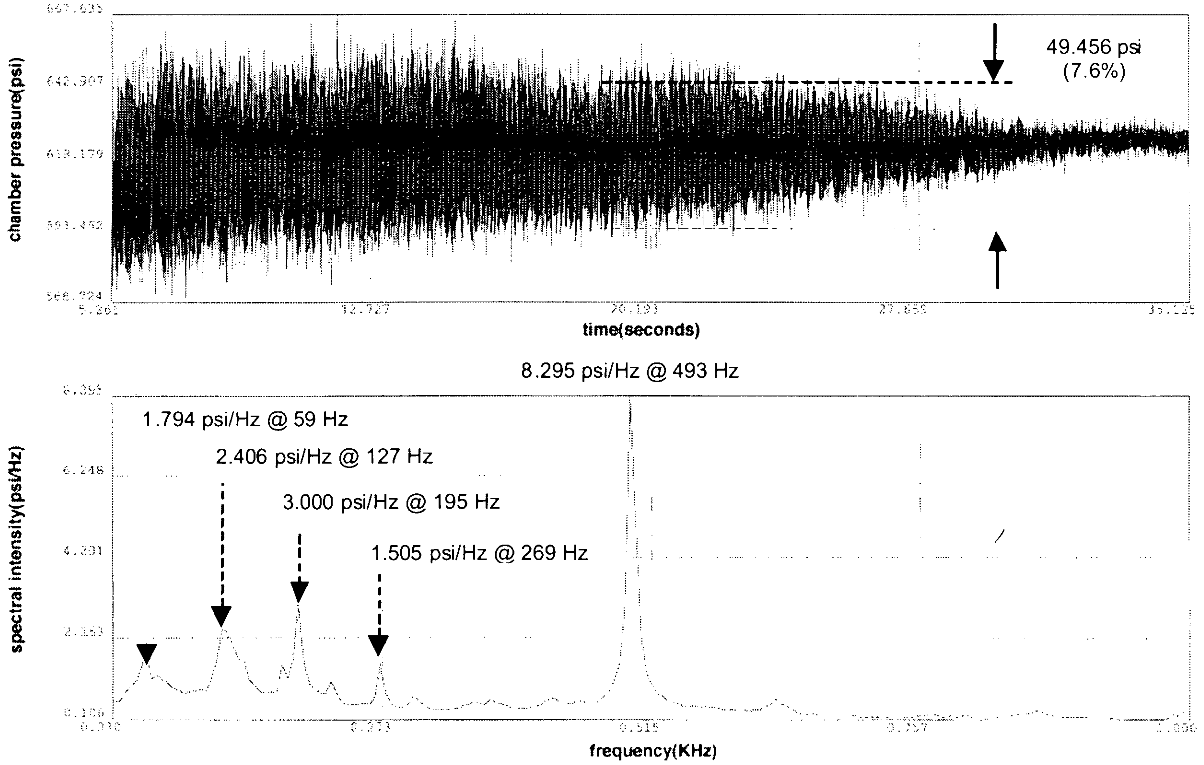

Figure-15: test-23 chamber pressure during the buzz-dominated phase of mainstage.

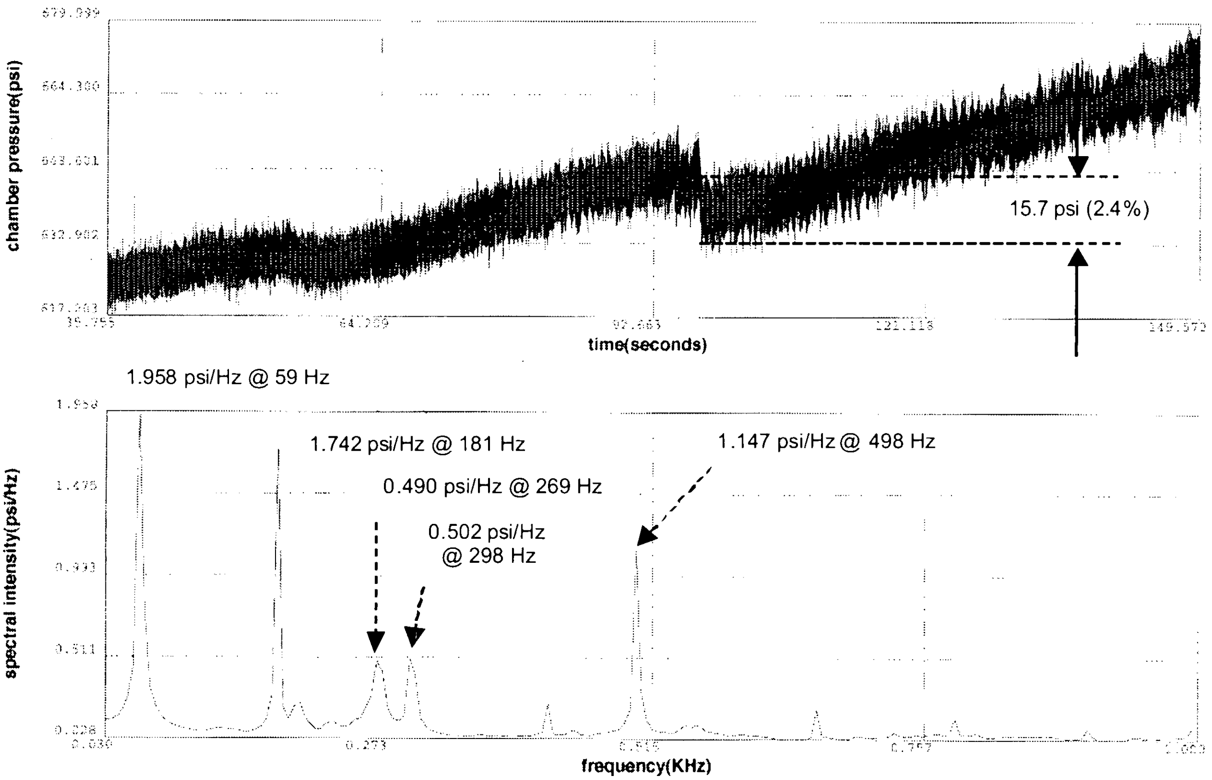

15.7 psi (2.4%)

1.958 psi/Hz @ 59 Hz

1.742 psi/Hz @ 181 Hz

0.490 psi/Hz @ 269 Hz

0.502 psi/Hz @ 298 Hz

1.147 psi/Hz @ 498 Hz

Figure-16: test-23 chamber pressure during the buzz-minimized phase of mainstage.

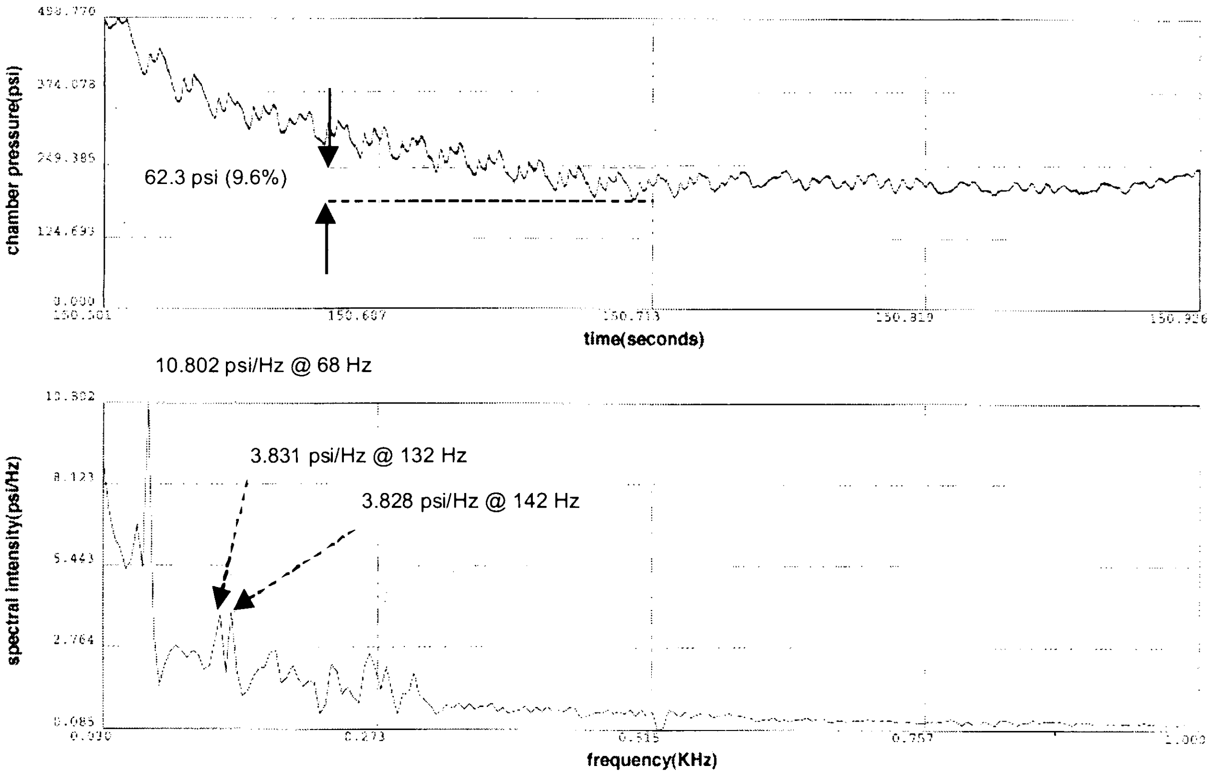

62.3 psi (9.6%)

10.802 psi/Hz @ 68 Hz

3.831 psi/Hz @ 132 Hz

3.828 psi/Hz @ 142 Hz

Figure-17: test-23 chamber pressure during the shutdown first sub-phase.

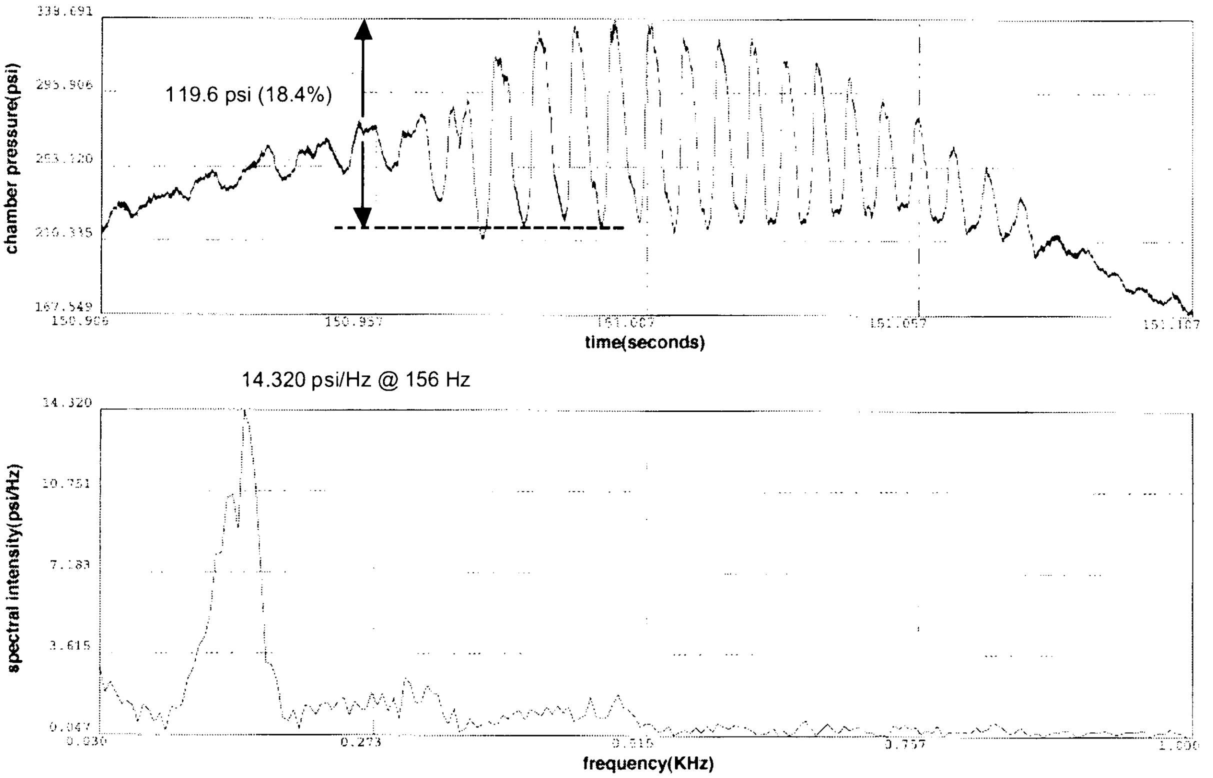

Figure-18: test-23 chamber pressure during the shutdown third sub-phase.

Consider the test-24 chamber pressure during the shut-down phase. As the TCA was powering-down from level-2 operation, chug was exhibited in several sub-phases. In the first shut-down sub-phase, chug was exhibited with an amplitude of about 12.4% of steady-state chamber pressure, with a spectral intensity of 13.809 psi/Hz (93.939 KPa/Hz) at a frequency of 78 Hz. The duration of chug in the first shut-down sub-phase was 404 milliseconds. In the second shut-down sub-phase, chug was exhibited with an amplitude of about 7.3% of steady-state chamber pressure, with a spectral intensity of 3.667 psi/Hz (24.946 KPa/Hz) at a frequency of 54 Hz and 6.203 psi/Hz (42.197 KPa/Hz) at 171 Hz. The duration of chug in the second shut-down sub-phase was 163 milliseconds. In the third shut-down sub-phase, chug was exhibited with an amplitude of about 30.7% of steady-state chamber pressure, with a spectral intensity of 20.954 psi/Hz (142.544 KPa/Hz) at a frequency of 161 Hz. The duration of chug in the third shut-down sub-phase was 148 milliseconds.

Consider the test-25 chamber pressure during the start-up phase. Chug was exhibited with an amplitude of about 29.5% of steady-state chamber pressure, with a spectral intensity of 31.203 psi/Hz (212.265 KPa/Hz) at a frequency of 205 Hz. The duration of this chug was about 158 milliseconds.

Consider the test-25 chamber pressure during the buzz-free phase. There was no buzz-dominated phase. As the TCA was operating at level-2 conditions, some low-frequency oscillations appeared in the spectrum with a magnitude of 2.202 psi/Hz (14.980 KPa/Hz) at 59 Hz, 4.434 psi/Hz (30.163 KPa/Hz) at 142 Hz, 2.444 psi/Hz (16.626 KPa/Hz) at 181 Hz, 1.585 psi/Hz (10.782 KPa/Hz) at 215 Hz, and 1.522 psi/Hz (10.354 KPa/Hz) at 293 Hz. The duration of this phase was about 3.845 seconds. The average amplitude was about 6.8% of the steady-state chamber pressure.

Consider the test-25 chamber pressure during the shut-down phase. As the TCA was powering-down from level-2 operation, chug was exhibited in several sub-phases. In the first shut-down sub-phase, chug was exhibited with an amplitude of about 24.7% of steady-state chamber pressure, with a spectral intensity of 37.995 psi/Hz (258.469 KPa/Hz) at a frequency of 78 Hz and 9.805 psi/Hz (66.701 KPa/Hz) at 151 Hz. The duration of chug in the first shut-down sub-phase was 263 milliseconds. In the second shut-down sub-phase, chug was exhibited with an amplitude of about 27.8% of steady-state chamber pressure, with a spectral intensity of 31.984 psi/Hz (217.578 KPa/Hz) at a frequency of 195 Hz. The duration of chug in the second shut-down sub-phase was 393 milliseconds. In the third shut-down sub-phase, chug was exhibited with an amplitude of about 31.7% of steady-state chamber pressure, with a spectral intensity of 33.415 psi/Hz (227.313 KPa/Hz) at a frequency of 176 Hz. The duration of chug in the third shut-down sub-phase was 144 milliseconds.

Consider the test-26 chamber pressure during the start-up phase. Chug was exhibited with an amplitude of about 25.9% of steady-state chamber pressure, with a spectral intensity of 24.689 psi/Hz (167.952 KPa/Hz) at a frequency of 186 Hz and 6.056 psi/Hz (41.197 KPa/Hz) at 376 Hz. The duration of this chug is about 187 milliseconds.

Consider the test-26 chamber pressure during the first sub-phase of the buzz-free phase. As the TCA was operating at level-2 conditions, some low-frequency oscillations appeared in the spectrum with a magnitude of 2.424 psi/Hz (16.490 KPa/Hz) at 59 Hz, 0.903 psi/Hz (6.143 KPa/Hz) at 142 Hz, 2.417 psi/Hz (16.442 KPa/Hz) at 181 Hz, and 0.736 psi/Hz (5.007 KPa/Hz) at 298 Hz. The duration of this phase was about 48 seconds. The maximum amplitude was about 6.4% of the steady-state chamber pressure.

Consider the test-26 chamber pressure during the second sub-phase of the buzz-free phase. As the TCA was still operating at level-2 conditions, some low-frequency oscillations appeared in the spectrum with a magnitude of 2.420 psi/Hz (16.463 KPa/Hz) at 59 Hz, 2.414 psi/Hz (16.422 KPa/Hz) at 181 Hz, and 0.431 psi/Hz (2.932 KPa/Hz) at 298 Hz. The duration of this phase was about 99 seconds. The average amplitude was about 2.4% of the steady-state chamber pressure.

Consider the test-26 chamber pressure during the shut-down phase. As the TCA was powering-down from level-2 operation, chug was exhibited in several sub-phases. In the first shut-down sub-phase, chug was exhibited with an amplitude of about 37.8% of steady-state chamber pressure, with a spectral intensity of 48.750 psi/Hz (331.633 KPa/Hz) at a frequency of 73 Hz, 11.885 psi/Hz (80.850 KPa/Hz) at 151 Hz, and 5.445 psi/Hz (37.041 KPa/Hz) at 225 Hz. The duration of chug in the first shut-down sub-phase was 567 milliseconds. In the second shut-down sub-phase, chug was exhibited with an amplitude of about 9.9% of steady-state chamber pressure, with a spectral intensity of 24.486 psi/Hz (166.571 KPa/Hz) at a frequency of 63 Hz and 11.974 psi/Hz at (81.456 KPa/Hz) 176 Hz. The duration of chug in the second shut-down sub-phase was 126 milliseconds. In the third shut-down sub-phase, chug was exhibited with an amplitude of about 36.2% of steady-state chamber pressure, with a spectral intensity of 27.069 psi/Hz (184.143 KPa/Hz) at a frequency of 156 Hz. The duration of chug in the third shut-down sub-phase was 159 milliseconds.

SUMMARY

For the Fastrac TCA, tested at MSFC test stand 116, the injector pressure drops were 19% and 20% on the RP-1 and LOX sides, respectively. Using these pressure drops, a linear analysis was conducted to determine the low-frequency combustion stability characteristics of the TCA combined with the RP-1 and LOX feed systems downstream of the venturies. This analysis was only valid when making predictions of low-frequency combustion stability during mainstage operation only. The most obvious result of this analysis was that the chamber pressure oscillations were stable. The low-frequency combustion stability was not very sensitive to changes in $\Delta P_F/P_C$. According to figure-8, $\Delta P_F/P_C$ could be lowered to below 4% without chug being exhibited. However, The low-frequency combustion stability was more sensitive to changes in $\Delta P_O/P_C$. According to figure-8, $\Delta P_O/P_C$ could be lowered to about 10% without chug being exhibited. Unfortunately, special testing to verify the sensitivity of low-frequency combustion stability to injector pressure drops was never performed. Additionally, these pressure oscillations would occur in the TCA and RP-1 and LOX feed systems at a frequency of 65 Hz and would be damped to 50% of their initial amplitude in about 10 milliseconds. The maximum allowable damp time was about 155 milliseconds.

For the Fastrac flight engine, tested at SSC, the injector pressure drops were unchanged at 19% and 20% on the RP-1 and LOX sides, respectively. Using these pressure drops, the linear analysis was repeated to determine the low-frequency combustion stability characteristics of the flight engine consisting of the TCA combined with the RP-1 and LOX feed systems. For the flight engine, the propellant feedlines were shortened according to flight engine design in figures 9 and 10. Additionally, in the analysis, the venturis were not replaced by pumps. The result of this analysis was that the chamber pressure oscillations were stable. According to figure-11, the low-frequency combustion stability was insensitive to changes in $\Delta P_F/P_C$ above $\Delta P_O/P_C = 10\%$. Also, low-frequency combustion stability was insensitive to changes in $\Delta P_O/P_C$ below $\Delta P_F/P_C = 20\%$. Unfortunately, the frequency and damp time of these pressure oscillations that would occur in the TCA and in the RP-1 and LOX feed systems of the flight engine were indeterminable.

In order to convert from a pressure-fed TCA to a pump-fed TCA, at the least, the propellant feedlines were shortened. The effect of shortening the propellant feedlines on low-frequency combustion instability was illustrated in figure-12. Shortening the propellant feedlines caused the neutral stability boundary to curve downward for low values of $\Delta P_F/P_C$, thereby increasing the region of stable combustion. In the following appendix, equations 13, 33, and 36 indicates that decreasing the propellant feedline volumes results in “stiffening” the propellant feed system. This is a stabilizing effect.

The experimental data from tests 23 through 26 indicated that during mainstage, low-frequency chamber pressure oscillations were present. Typical frequencies consisted of the fundamental frequency of 60 Hz with its first and second harmonics at 180 Hz and 300 Hz, respectively. An additional group of peaks in the spectrum occurred at frequencies of 127 Hz, 132 Hz, and 142 Hz. A second group of peaks in the spectrum occurred at the frequencies of 195 Hz and 215 Hz. Finally, a third group of peaks in the spectrum occurred at the frequencies of 269 Hz and 273 Hz. However, the spectral intensity of these peaks were greatly overshadowed by the peak that was at 500 Hz in tests 23 and 24. Once the 500 Hz intermediate frequency combustion instability was eliminated in tests 25 and 26, the low-frequency pressure oscillations remained but resulted in low amplitudes that did not raise any concerns about combustion instability during mainstage.

The experimental data from tests 23 through 26 indicated that during start-up, chug was present. The duration of the chug was from 139 to 187 milliseconds. In the chamber pressure frequency spectrum, there was a peak at a frequency of 186 Hz. Also, there was a typical group of peaks which had frequencies at 195 Hz and 205 Hz. Finally, there was a peak with a frequency of 376 Hz. Note that the peak at 376 Hz was secondary in spectral intensity and was very close to the first harmonic of 186 Hz.

The experimental data from tests 23 through 26 indicated that during shutdown, chug was present. The duration of the chug was from 601 to 852 milliseconds. In the chamber pressure frequency spectrum, there were peaks at the frequencies of 78 Hz, 151 Hz, and 225 Hz during the first shutdown sub-phase. Note that the peaks at 151 Hz and 225 Hz are close to the first and second harmonics of 78 Hz, respectively. Also, during the first shutdown sub-phase, there were peaks at the frequencies of 68 Hz, 132 Hz, and 142 Hz. Note that 132 Hz is close to the first harmonic of 68 Hz. During the second shutdown sub-phase, there were a group of peaks at the frequencies of 54 Hz and 63 Hz. Note that these frequencies are close to 60 Hz. Also, during the second shutdown sub-phase there were another group of peaks at 171 Hz and 176 Hz. Note that these frequencies are close to 180 Hz, the first harmonic of 60 Hz. Finally, during the second shutdown sub-phase there was a peak at 195 Hz. During the third shutdown sub-phase there were peaks at the frequencies of 156 Hz, 161 Hz, and 176 Hz.

While the analysis indicated damped pressure oscillations at 65 Hz, the test data indicated peaks at low spectral intensity at 60 Hz. This leads to one of two possibilities. One possibility is that the analysis accurately predicted a frequency of pressure oscillation. The other possibility is that this close agreement is merely coincidental. The appearance of the 60 Hz oscillations with the respective harmonics is due to poor transducer cable connections resulting in “ground looping[7]” or poor grounding of the cable. The causes of ground looping may be numerous. One cause may be moisture trapped between the transducer and cable lead.

ACKNOWLEDGMENTS

The authors would like to acknowledge and thank Dr. John J. Hutt (NASA/MSFC), team leader of the Fastrac Combustion Devices Team, whose contributions were crucial during the design of the Fastrac injector and whose direction was crucial during the Fastrac TCA performance testing. Dr. Hutt originally requested the development of this analysis.

REFERENCES

1) "Guidelines For Combustion Stability Specifications And Verification Procedures For Liquid Propellant Rocket Engines", CPIA Publication-247, page-4, 1973.

2) "Elimination of High-Frequency Combustion Instability in the Fastrac Engine Thrust Chamber", M. Rocker and T.E. Nesman, presented at the 1999 JANNAF Joint Meeting of the Combustion, Airbreathing Propulsion, and Propulsion System Hazards Subcommittees in Cocoa Beach, Florida, 1999.

3) "Elimination of Intermediate-Frequency Combustion Stability of the Fastrac Engine Thrust Chamber", M. Rocker and T. E. Nesman, to be published, 2001.

4) "Analysis of Chugging in Liquid-Bipropellant Rocket Engines Using Propellants with Different Vaporization Rates", L.M. Wenzel and J.R. Szuch, NASA TN D-3080, 1965.

5) "Rocket Propulsion Elements", fourth edition, G.P. Sutton and D.M. Ross, pages 276-277, 1976.

6) "Liquid Propellant Rocket Combustion Instability", NASA SP-194, editors: D.T. Harrje and F.H. Reardon, page-269, 1972.

7) Private Communication, R.A. Hewitt, Aerojet, June 14, 2001.

APPENDIX: REVIEW OF MODEL FORMULATION

The formulation of the model by which low-frequency combustion instability predictions were performed began with the modeling of the liquid propellant feed system. A feed system element was defined, as illustrated in figure-19. The feed system element had two components, a feedline segment and a flow control device. The feedline segment was represented by a volume of fluid. While the pressure within the feedline segment was assumed to vary with time, it did not vary in space. Additionally, the feedline segment received fluid from upstream and lost fluid through the flow control device downstream. The flow control device was represented by a flow constriction between two feedline segments. It was understood that the flow control device could have been an orifice, valve, or anything across which a pressure drop occured. Within the flow control device, the flow rate varied with time but was constant along the length of the flow control device.

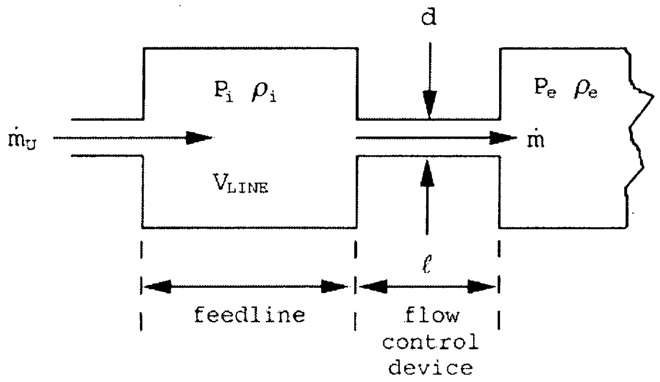

Figure-19: feedline element schematic.

Within the feedline segment, the fluid behavior was governed by the conservation of mass:

$$\frac{\mathrm{d}}{\mathrm{dt}}\oiiint \rho \mathrm{dV} + \oiint \rho \boldsymbol{V} \bullet \boldsymbol{N} \mathrm{ds} = 0 \ . \tag{5}$$

After applying conservation of mass to the feedline segment in figure-19, equation-5 became:

$$\mathrm{V}_{\mathrm{LINE}}\frac{\mathrm{d}\rho_{\mathrm{i}}}{\mathrm{dt}} = \dot{\mathrm{m}}_{\mathrm{U}} - \dot{\mathrm{m}} \ . \tag{6}$$

Fluid density is usually presented as a function of pressure and temperature:

$$\rho_{\mathrm{i}} = \rho(\mathrm{P}_{\mathrm{i}},\mathrm{T}_{\mathrm{i}}) \ . \tag{7}$$

However, since isothermal flow was assumed, equation-7 became:

$$\rho_{\mathrm{i}} = \rho(\mathrm{P}_{\mathrm{i}}) \ . \tag{8}$$

Therefore, the term on the left-hand side of equation-6 became:

$$\frac{\mathrm{d}\rho_{\mathrm{i}}}{\mathrm{dt}} = \frac{\mathrm{d}\rho_{\mathrm{i}}}{\mathrm{dP}_{\mathrm{i}}}\frac{\mathrm{dP}_{\mathrm{i}}}{\mathrm{dt}} = \rho'(\mathrm{P}_{\mathrm{i}})\frac{\mathrm{dP}_{\mathrm{i}}}{\mathrm{dt}} \ . \tag{9}$$

Since the fluid was assumed to be a liquid at constant temperature, density was assumed to vary linearly as a function of pressure. Therefore:

$$\rho'(\mathrm{P}_{\mathrm{i}}) = \mathrm{constant} \ . \tag{10}$$

Therefore, substituting equation-9 into equation-6 and linearizing about steady-state conditions gave:

$$\mathrm{V}_{\mathrm{LINE}}\rho'(\overline{\mathrm{P}}_{\mathrm{i}})\frac{\mathrm{dP}_{\mathrm{i}}'}{\mathrm{dt}} = \dot{\mathrm{m}}_{\mathrm{U}}' - \dot{\mathrm{m}}' \ . \tag{11}$$

Scaling equation-11 by the steady-state flow rate and steady-state chamber pressure gave:

$$\mathrm{C}\frac{\mathrm{d}}{\mathrm{dt}}\left(\frac{\mathrm{P}_{\mathrm{i}}'}{\overline{\mathrm{P}}_{\mathrm{C}}}\right) = \frac{\dot{\mathrm{m}}_{\mathrm{U}}'}{\overline{\dot{\mathrm{m}}}} - \frac{\dot{\mathrm{m}}'}{\overline{\dot{\mathrm{m}}}} \ . \tag{12}$$

Where the scaled capacitance was defined as:

$$C = \frac{\overline{P}_C V_{LINE} \rho'\left(\overline{P}_i\right)}{\overline{\dot{m}}} \quad . \tag{13}$$

It was determined that the scaled capacitance had the units of seconds. Note that for the steady-state flow rates:

$$\overline{\dot{m}}_U = \overline{\dot{m}} \quad . \tag{14}$$

Within the flow control device, fluid behavior was governed by the conservation of momentum of Newton's second law of motion:

$$\frac{d}{dt}\oiiint \rho \boldsymbol{V} dV + \oiint \rho \boldsymbol{V}(\boldsymbol{V} \bullet \boldsymbol{N}) ds = -\oiint P\boldsymbol{N} ds + \iint \tau_w ds \quad . \tag{15}$$

Where for the first term on the left-hand side of equation-15:

$$\frac{d}{dt}\oiiint \rho \boldsymbol{V} dV = \frac{d}{dt}\int_0^{\ell} \rho u A dx \; \boldsymbol{e}_x = \ell \frac{d\dot{m}}{dt} \; \boldsymbol{e}_x \quad . \tag{16}$$

For the second term on the left-hand side of equation-15:

$$\oiint \rho \boldsymbol{V}(\boldsymbol{V} \bullet \boldsymbol{N}) ds = \left(\rho_e u_e^2 - \rho_i u_i^2\right) A \; \boldsymbol{e}_x = \left(\frac{1}{\rho_e} - \frac{1}{\rho_i}\right)\frac{\dot{m}^2}{A} \; \boldsymbol{e}_x \quad . \tag{17}$$

For the first term on the right-hand side of equation-15:

$$\oiint P\boldsymbol{N} ds = \left(P_e - P_i\right) A \; \boldsymbol{e}_x \quad . \tag{18}$$

And, for the second term on the right-hand side of equation-15:

$$\iint \tau_w ds = -\frac{f}{4}\frac{\rho_{avg} u_{avg}^2}{2} \ell \pi d \; \boldsymbol{e}_x = -\frac{f}{4}\frac{1}{2\rho_{avg}}\left(\frac{\dot{m}}{A}\right)^2 \ell \pi d \; \boldsymbol{e}_x \quad . \tag{19}$$

By substituting equations-16, 17, 18, and 19 into equation-15, conservation of momentum has been applied to the flow control device in figure-19. Therefore, equation-15 became:

$$\ell \frac{d\dot{m}}{dt} + \left(\frac{1}{\rho_e} - \frac{1}{\rho_i}\right)\frac{\dot{m}^2}{A} = \left(P_i - P_e\right) A - \frac{f}{4}\frac{1}{2\rho_{avg}}\left(\frac{\dot{m}}{A}\right)^2 \ell \pi d \quad . \tag{20}$$

The cross-sectional area of the flow control device and the average density across the flow control device was defined, respectively, by:

$$A = \frac{\pi d^2}{4} \ , \ 2\rho_{avg} = \rho_i + \rho_e \ . \tag{21), (22}$$

Dividing equation-20 by the cross-sectional area, and then substituting in equations 21 and 22 gave:

$$\frac{\ell}{A}\frac{d\dot{m}}{dt} + \left(\frac{1}{\rho_e} - \frac{1}{\rho_i}\right)\left(\frac{\dot{m}}{A}\right)^2 = P_i - P_e - \frac{f\ell}{d}\frac{1}{\left(\rho_i + \rho_e\right)}\left(\frac{\dot{m}}{A}\right)^2 \ . \tag{23}$$

The flow control device loss coefficient was defined such that:

$$K_{loss} = \begin{cases} \dfrac{f\ell}{d} & : \text{fanno line} \\ K_{loss} & : \text{orifice, valve, etc.} \end{cases} \ . \tag{24}$$

Therefore, equation-24 became:

$$\frac{\ell}{A}\frac{d\dot{m}}{dt} + \left(\frac{1}{\rho_e} - \frac{1}{\rho_i}\right)\left(\frac{\dot{m}}{A}\right)^2 = P_i - P_e - \frac{K_{loss}}{\left(\rho_i + \rho_e\right)}\left(\frac{\dot{m}}{A}\right)^2 \ . \tag{25}$$

Linearizing equation-25 about the steady-state conditions gave the ordinary differential equation for the perturbation in flow rate:

$$\begin{aligned} &\frac{\ell}{A}\frac{d\dot{m}'}{dt} + \left\{\frac{1}{\bar{\rho}_e} - \frac{1}{\bar{\rho}_i} + \frac{K_{loss}}{\left(\bar{\rho}_i + \bar{\rho}_e\right)}\right\}\frac{2\bar{\dot{m}}\dot{m}'}{A^2} \\ &= \left\{1 - \frac{\rho'(\bar{P}_i)}{\bar{\rho}_i^2}\left(\frac{\bar{\dot{m}}}{A}\right)^2 + \frac{K_{loss}\rho'(\bar{P}_i)}{\left(\bar{\rho}_i + \bar{\rho}_e\right)^2}\left(\frac{\bar{\dot{m}}}{A}\right)^2\right\}P_i' \\ &- \left\{1 - \frac{\rho'(\bar{P}_e)}{\bar{\rho}_e^2}\left(\frac{\bar{\dot{m}}}{A}\right)^2 - \frac{K_{loss}\rho'(\bar{P}_e)}{\left(\bar{\rho}_i + \bar{\rho}_e\right)^2}\left(\frac{\bar{\dot{m}}}{A}\right)^2\right\}P_e' \ . \end{aligned} \tag{26}$$

In the process of linearizing equation-25, the steady-state momentum equation was obtained:

$$\frac{K_{loss}}{\left(\bar{\rho}_i + \bar{\rho}_e\right)}\left(\frac{\bar{\dot{m}}}{A}\right)^2 = \bar{P}_i - \bar{P}_e - \left(\frac{1}{\bar{\rho}_e} - \frac{1}{\bar{\rho}_i}\right)\left(\frac{\bar{\dot{m}}}{A}\right)^2 \ . \tag{27}$$

Substituting equation-27 into equation-26 and dividing through by the steady-state chamber pressure gave:

$$L\frac{d}{dt}\left(\frac{\dot{m}'}{\bar{\dot{m}}}\right) + R\frac{\dot{m}'}{\bar{\dot{m}}} = K_i\frac{P_i'}{\bar{P}_C} - K_e\frac{P_e'}{\bar{P}_C} \ . \tag{28}$$

Where the scaled inertance and the scaled resistance were respectively defined as:

$$L = \frac{\bar{\dot{m}}\ell}{\bar{P}_C A} \; , \; R = \frac{2\left(\bar{P}_i - \bar{P}_e\right)}{\bar{P}_C} \; . \tag{29), (30}$$

The units for the scaled inertance and scaled resistance were seconds, and dimensionless, respectively. The inlet convective-resistance was defined as:

$$K_i = 1 - \frac{\rho'\left(\bar{P}_i\right)}{\bar{\rho}_i^2}\left(\frac{\bar{\dot{m}}}{A}\right)^2 + \frac{\rho'\left(\bar{P}_i\right)}{\left(\bar{\rho}_i + \bar{\rho}_e\right)}\left\{\bar{P}_i - \bar{P}_e - \left(\frac{1}{\bar{\rho}_e} - \frac{1}{\bar{\rho}_i}\right)\left(\frac{\bar{\dot{m}}}{A}\right)^2\right\} . \tag{31}$$

Also, the exit convective-resistance was defined as:

$$K_e = 1 - \frac{\rho'\left(\bar{P}_e\right)}{\bar{\rho}_e^2}\left(\frac{\bar{\dot{m}}}{A}\right)^2 - \frac{\rho'\left(\bar{P}_e\right)}{\left(\bar{\rho}_i + \bar{\rho}_e\right)}\left\{\bar{P}_i - \bar{P}_e - \left(\frac{1}{\bar{\rho}_e} - \frac{1}{\bar{\rho}_i}\right)\left(\frac{\bar{\dot{m}}}{A}\right)^2\right\} . \tag{32}$$

The units for both the inlet and exit convective-resistance were dimensionless. Differentiating equation-28, and substituting in equation-12 gave:

$$L\frac{d^2}{dt^2}\left(\frac{\dot{m}'}{\bar{\dot{m}}}\right) + R\frac{d}{dt}\left(\frac{\dot{m}'}{\bar{\dot{m}}}\right) + \frac{K_i}{C}\frac{\dot{m}'}{\bar{\dot{m}}} = \frac{K_i}{C}\frac{\dot{m}'_U}{\bar{\dot{m}}} - K_e\frac{d}{dt}\left(\frac{P'_e}{\bar{P}_C}\right) . \tag{33}$$

Combined with equation-12:

$$C\frac{d}{dt}\left(\frac{P'_i}{\bar{P}_C}\right) = \frac{\dot{m}'_U}{\bar{\dot{m}}} - \frac{\dot{m}'}{\bar{\dot{m}}} \; , \tag{34}$$

these two ordinary differential equations describe the fluid flow inside of the feed system element.

Equation-33 is dynamically similar to two analogous systems. The first system is electrical and the second system is mechanical. For the electrical system, the governing equation was:

$$L\frac{d^2Q}{dt^2} + R\frac{dQ}{dt} + \frac{1}{C}Q = \frac{dE}{dt} . \tag{35}$$

Where Q was the electronic flow rate or current. By comparing equation-35 to equation-33, one concluded that L was either the inductance in equation-35 or the scaled inertance in equation-33. Also, R was the scaled resistance in equation-33 and the resistance in equation-35. Finally, C was the scaled capacitance in both equation-33 and the capacitance in equation-35. For the second system, the governing equation was:

$$m\frac{d^2x}{dt^2} + c\frac{dx}{dt} + kx = f(t) . \tag{36}$$

Where x was the displacement of mass-m. By comparing equation-36 to equation-33, one concluded that m, which was the linear inertia or mass in equation-36, was analogous to the inertance-L in equation-33. Also, c, which was the damping coefficient in equation-36, was analogous to the scaled resistance-R in equation-33. Finally, k, which was the stiffness in equation-36, was analogous to 1/C, where C was the scaled capacitance in equation-33. A large scaled resistance in equation-33 would contribute to the elimination of oscillations in the feed system. Since the stiffness in equation-36 is inversely proportional to the scaled capacitance in equation-33, A feed system with a large scaled capacitance will have a low stiffness. Such a feed system was said to be "soft". A soft feed system will have either large feedline volumes, feedline volumes filled with highly compressible fluids, or both. A feed system with a low scaled capacitance will have a high stiffness. Such a feed system is said to be "stiff". A stiff feed system will have small feedline volumes, be filled with a low compressibility fluid, or both.

It was assumed that the solutions of equations-33 and 34 would be exponential functions:

$$\dot{m}'(t) = \dot{M}(s)e^{st}, \quad \dot{m}'_U(t) = \dot{M}_U(s)e^{st} ,$$

(37), (38)

$$P'_i(t) = P_i(s)e^{st}, \quad P'_e(t) = P_e(s)e^{st} .$$

(39), (40)

The exponential function exhibited sinusoidal behavior with damping when s was defined as:

$$s = \lambda + j\omega \quad , \quad j = \sqrt{-1} .$$

(41), (42)

Substituting equations-37, 38, 39, and 40 into equations-33 and 34 gave:

$$\left(Ls^2 + Rs + \frac{K_i}{C}\right)\frac{\dot{M}(s)}{\bar{\dot{m}}} = \frac{K_i}{C}\frac{\dot{M}_U(s)}{\bar{\dot{m}}} - K_e s\frac{P_e(s)}{\bar{P}_c} ,$$

(43)

$$Cs\frac{P_i(s)}{\bar{P}_c} = \frac{\dot{M}_U(s)}{\bar{\dot{m}}} - \frac{\dot{M}(s)}{\bar{\dot{m}}} .$$

(44)

After the equations of fluid motion had been established for a single feed system element, consisting of a feedline segment and a flow control device, the equation set describing the dynamics of a single propellant feed system consisting of a series of several feed system elements was established. The model of a single propellant feed system is presented in figure-20:

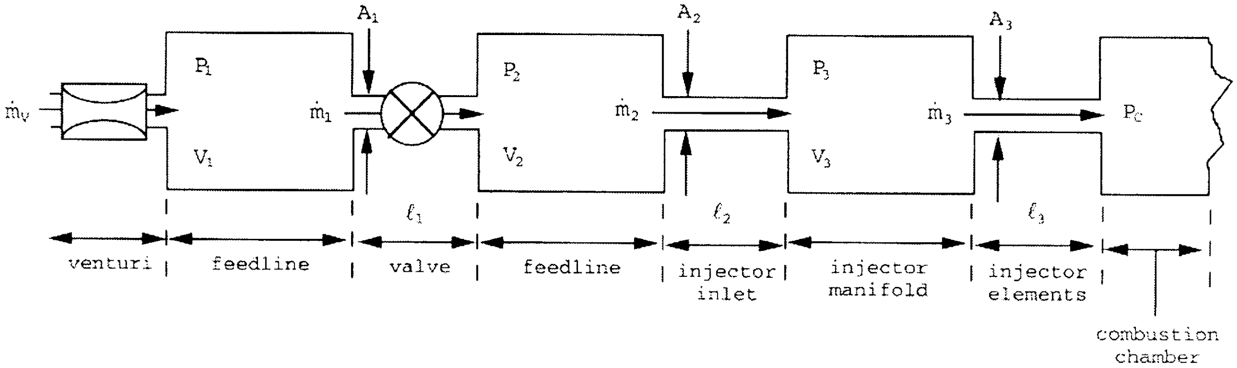

Figure-20: single propellant feed system schematic.

The three feedline elements linked in series model the portion of the feed system downstream of the venturi and upstream of the combustion chamber. This resulted in a set of three momentum equations, one for each of the three elements:

$$\left(L_1 s^2 + R_1 s + \frac{K_{i1}}{C_1}\right)\frac{\dot{M}_1(s)}{\bar{\dot{m}}} = \frac{K_{i1}}{C_1}\frac{\dot{M}_V(s)}{\bar{\dot{m}}} - K_{e1} s \frac{P_2(s)}{\bar{P}_C} , \tag{45}$$

$$\left(L_2 s^2 + R_2 s + \frac{K_{i2}}{C_2}\right)\frac{\dot{M}_2(s)}{\bar{\dot{m}}} = \frac{K_{i2}}{C_2}\frac{\dot{M}_1(s)}{\bar{\dot{m}}} - K_{e2} s \frac{P_3(s)}{\bar{P}_C} , \tag{46}$$

$$\left(L_3 s^2 + R_3 s + \frac{K_{i3}}{C_3}\right)\frac{\dot{M}_3(s)}{\bar{\dot{m}}} = \frac{K_{i3}}{C_3}\frac{\dot{M}_2(s)}{\bar{\dot{m}}} - K_{e3} s \frac{P_C(s)}{\bar{P}_C} . \tag{47}$$

Where for the mass equations:

$$C_2 s \frac{P_2(s)}{\bar{P}_C} = \frac{\dot{M}_1(s)}{\bar{\dot{m}}} - \frac{\dot{M}_2(s)}{\bar{\dot{m}}} , \tag{48}$$

$$C_3 s \frac{P_3(s)}{\bar{P}_C} = \frac{\dot{M}_2(s)}{\bar{\dot{m}}} - \frac{\dot{M}_3(s)}{\bar{\dot{m}}} . \tag{49}$$

Equations 48 and 49 were substituted into equations 45 and 46, respectively. The equations became:

$$\begin{Bmatrix} \alpha_{11}(s) & \alpha_{12} & 0 \\ \alpha_{21} & \alpha_{22}(s) & \alpha_{23} \\ 0 & \alpha_{32} & \alpha_{33}(s) \end{Bmatrix} \begin{Bmatrix} Y_1(s) \\ Y_2(s) \\ Y_3(s) \end{Bmatrix} = \begin{Bmatrix} 0 \\ 0 \\ \gamma_3(s) \end{Bmatrix} . \tag{50}$$

Where for the α's:

$$\alpha_{11}(s) = L_1 s^2 + R_1 s + \frac{K_{i1}}{C_1} + \frac{K_{e1}}{C_2} , \tag{51}$$

$$\alpha_{12} = -\frac{K_{e1}}{C_2} , \quad \alpha_{21} = -\frac{K_{i2}}{C_2} , \tag*{(52), (53)}$$

$$\alpha_{22}(s) = L_2 s^2 + R_2 s + \frac{K_{i2}}{C_2} + \frac{K_{e2}}{C_3} , \tag{54}$$

$$\alpha_{23} = -\frac{K_{e2}}{C_3} , \quad \alpha_{32} = -\frac{K_{i3}}{C_3} ,$$

(55), (56)

$$\alpha_{33}(s) = L_3 s^2 + R_3 s + \frac{K_{i3}}{C_3} .$$

(57)

Also, for the admittances:

$$Y_1(s) = \frac{\dot{M}_1(s)}{P_C(s)} \frac{\overline{P}_C}{\overline{\dot{m}}} , \quad Y_2(s) = \frac{\dot{M}_2(s)}{P_C(s)} \frac{\overline{P}_C}{\overline{\dot{m}}} , \quad Y_3(s) = \frac{\dot{M}_3(s)}{P_C(s)} \frac{\overline{P}_C}{\overline{\dot{m}}} .$$

(58), (59), (60)

Finally, for the chamber pressure perturbation forcing function:

$$\gamma_3(s) = -K_{e3} s .$$

(61)

Note that for the flow rate perturbation through the venturi:

$$\dot{M}_V(s) = 0 .$$

(62)

Solving equation-50 for the admittances gave:

$$Y_3(s) = \frac{\gamma_3}{\alpha_{33} + \dfrac{\alpha_{11}\alpha_{23}\alpha_{32}}{(\alpha_{21}\alpha_{12} - \alpha_{11}\alpha_{22})}} .$$

(63)

The α's and γ_3 were assumed to correspond to the oxizider feed system. Equation-63 became:

$$Y_{3O}(s) = \frac{\gamma_3}{\alpha_{33} + \dfrac{\alpha_{11}\alpha_{23}\alpha_{32}}{(\alpha_{21}\alpha_{12} - \alpha_{11}\alpha_{22})}} = Y_O(s) .$$

(64)

Similarly, the β's and δ_3 were assumed to correspond to the fuel feed system. Therefore, equation-65 gave:

$$Y_{3F}(s) = \frac{\delta_3}{\beta_{33} + \dfrac{\beta_{11}\beta_{23}\beta_{32}}{(\beta_{21}\beta_{12} - \beta_{11}\beta_{22})}} = Y_F(s) .$$

(65)

In figure-10, schematic of the combustion chamber is presented. First, the propellants undergo injection into the chamber. Second, the propellants are atomized, vaporized, mixed, and undergo combustion or burning to produce combustion products. Third, the combustion products are expanded through the nozzle. In the combustion chamber, the combustion products were assumed to behave as an ideal gas. Additionally, the pressure and temperature in the combustion chamber behaved as a function of time only, and did not vary in space. Therefore, conservation of mass with the nozzle gas flow rate gave:

$$\frac{V_C}{R}\frac{d}{dt}\left(\frac{P_C}{T_C}\right) = \dot{m}_B(t) - \dot{m}_N(t), \quad \dot{m}_N = \left(\frac{2}{\gamma+1}\right)^{\frac{1}{2}\left(\frac{\gamma+1}{\gamma-1}\right)} \sqrt{\frac{\gamma}{RT_C}}\,P_C A_T \ .$$

(66), (67)

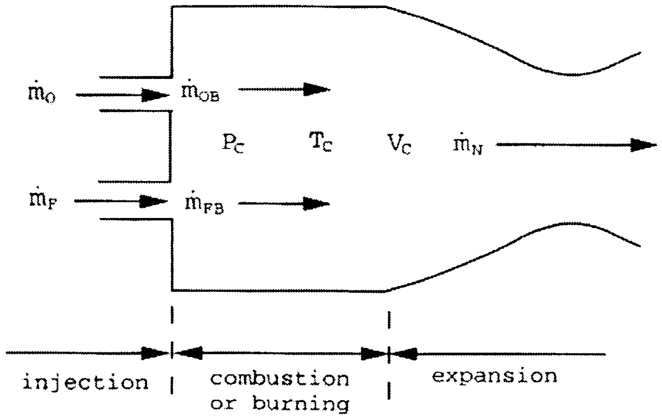

Figure-21: schematic of rocket engine combustion chamber.

Where for the propellant burning rate and the mixture ratio:

$$\dot{m}_B = \dot{m}_{OB} + \dot{m}_{FB}, \quad r = \frac{\dot{m}_{OB}}{\dot{m}_{FB}} \ .$$

(68), (69)

Substituting equations 67, 68, and 69 into equation-66 and the linearizing equation-66 about the steady-state conditions gave the ordinary differential equation for the perturbations in chamber pressure and chamber temperature:

$$\frac{\bar{\rho}_C V_C}{\bar{\dot{m}}}\frac{d}{dt}\left(\frac{P'_C}{\bar{P}_C}\right) - \frac{\bar{\rho}_C V_C}{\bar{\dot{m}}}\frac{d}{dt}\left(\frac{T'_C}{\bar{T}_C}\right)$$

$$= \left(\frac{\bar{r}}{\bar{r}+1}\right)\frac{\dot{m}'_{OB}}{\bar{\dot{m}}_{OB}} + \left(\frac{1}{\bar{r}+1}\right)\frac{\dot{m}'_{FB}}{\bar{\dot{m}}_{FB}} - \left(\frac{P'_C}{\bar{P}_C} - \frac{1}{2}\frac{T'_C}{\bar{T}_C}\right) \ .$$

(70)

The chamber temperature is a function of both chamber pressure and mixture ratio. However, it is regarded as being a strong function of mixture ratio only:

$$T_C = T_C(r) \ .$$

(71)

The Taylor's series expansion of the chamber temperature about steady-state conditions gave:

$$T_C(r) = T_C(\bar{r} + r') = T_C(\bar{r}) + r'\overline{\frac{\partial T_C}{\partial r}} + \frac{1}{2\,!}(r')^2\,\overline{\frac{\partial^2 T_C}{\partial r^2}} + \;.\;.\;. \tag{72}$$

Linearizing gave:

$$T_C(r) = \bar{T}_C + T_C' = T_C(\bar{r}) + r'\overline{\frac{\partial T_C}{\partial r}} \;. \tag{73}$$

Therefore, for the perturbation in chamber temperature:

$$\frac{T_C'}{\bar{T}_C} = \frac{\bar{r}}{\bar{T}_C}\overline{\frac{\partial T_C}{\partial r}}\frac{r'}{\bar{r}} \;. \tag{74}$$

From the linearization of equation-69, perturbation in mixture ratio was determined to be:

$$\frac{r'}{\bar{r}} = \frac{\dot{m}_{OB}'}{\bar{\dot{m}}_{OB}} - \frac{\dot{m}_{FB}'}{\bar{\dot{m}}_{FB}} \;. \tag{75}$$

Substituting equation-75 into equation-74 gave:

$$\frac{T_C'}{\bar{T}_C} = \frac{\bar{r}}{\bar{T}_C}\overline{\frac{\partial T_C}{\partial r}}\left(\frac{\dot{m}_{OB}'}{\bar{\dot{m}}_{OB}} - \frac{\dot{m}_{FB}'}{\bar{\dot{m}}_{FB}}\right) \;. \tag{76}$$

Substituting equation-76 into equation-70 gave:

$$\begin{aligned}\frac{\bar{\rho}_C V_C}{\bar{\dot{m}}}\frac{d}{dt}\left(\frac{P_C'}{\bar{P}_C}\right) + \frac{P_C'}{\bar{P}_C} = {} & \frac{\bar{\rho}_C V_C}{\bar{\dot{m}}}\frac{\bar{r}}{\bar{T}_C}\overline{\frac{\partial T_C}{\partial r}}\frac{d}{dt}\left(\frac{\dot{m}_{OB}'}{\bar{\dot{m}}_{OB}}\right) - \frac{\bar{\rho}_C V_C}{\bar{\dot{m}}}\frac{\bar{r}}{\bar{T}_C}\overline{\frac{\partial T_C}{\partial r}}\frac{d}{dt}\left(\frac{\dot{m}_{FB}'}{\bar{\dot{m}}_{FB}}\right) \\ & + \left\{\left(\frac{\bar{r}}{\bar{r}+1}\right) + \frac{1}{2}\frac{\bar{r}}{\bar{T}_C}\overline{\frac{\partial T_C}{\partial r}}\right\}\frac{\dot{m}_{OB}'}{\bar{\dot{m}}_{OB}} + \left\{\left(\frac{1}{\bar{r}+1}\right) - \frac{1}{2}\frac{\bar{r}}{\bar{T}_C}\overline{\frac{\partial T_C}{\partial r}}\right\}\frac{\dot{m}_{FB}'}{\bar{\dot{m}}_{FB}} \;.\end{aligned} \tag{77}$$

For the perturbations in the oxidizer and fuel burning rates:

$$\dot{m}_{OB}'(t) = \dot{m}_O'(t - \tau_O) \;,\; \dot{m}_{FB}'(t) = \dot{m}_F'(t - \tau_F) \;. \tag{78), (79}$$

Equations 78 and 79 stated that the burning rate of a given propellant at some instant t was not equal to the injection flow rate of the given propellant at the same instant. But the burning rate at some instant t was equal to the injection flow rate at the prior instant t-τ_O or t-τ_F for the oxidizer or fuel, respectively. For the derivative with respect to time of the perturbations in the propellant flow rates:

$$\frac{d}{dt}\dot{m}'_{OB}(t) = \frac{d}{d(t-\tau_O)}\dot{m}'_O(t-\tau_O)\frac{d}{dt}(t-\tau_O) = \frac{d}{d(t-\tau_O)}\dot{m}'_O(t-\tau_O) \ ,$$

$$\frac{d}{dt}\dot{m}'_{OF}(t) = \frac{d}{d(t-\tau_F)}\dot{m}'_F(t-\tau_F)\frac{d}{dt}(t-\tau_F) = \frac{d}{d(t-\tau_F)}\dot{m}'_F(t-\tau_F) \ .$$

(80), (81)

For the combustion chamber flush/fill time, the steady-state oxidizer flow, fuel flow, and total propellant rates:

$$\tau_C = \frac{\bar{\rho}_C V_C}{\bar{\dot{m}}} \ , \ \bar{\dot{m}}_{OB} = \bar{\dot{m}}_O \ , \ \bar{\dot{m}}_{FB} = \bar{\dot{m}}_F \ , \ \bar{\dot{m}} = \bar{\dot{m}}_O + \bar{\dot{m}}_F \ .$$

(82), (83), (84), (85)

Substituting equations 78 through 84 into equation-77 gave:

$$\begin{aligned}
\tau_C \frac{d}{dt}\left(\frac{P'_C}{\bar{P}_C}\right) + \frac{P'_C}{\bar{P}_C} = \ & \tau_C \frac{\bar{r}}{\bar{T}_C}\overline{\frac{\partial T_C}{\partial r}}\frac{d}{d(t-\tau_O)}\left\{\frac{\dot{m}'_O(t-\tau_O)}{\bar{\dot{m}}_O}\right\} \\
& - \tau_C \frac{\bar{r}}{\bar{T}_C}\overline{\frac{\partial T_C}{\partial r}}\frac{d}{d(t-\tau_F)}\left\{\frac{\dot{m}'_F(t-\tau_F)}{\bar{\dot{m}}_F}\right\} \\
& + \left\{\left(\frac{\bar{r}}{\bar{r}+1}\right) + \frac{1}{2}\frac{\bar{r}}{\bar{T}_C}\overline{\frac{\partial T_C}{\partial r}}\right\}\frac{\dot{m}'_O(t-\tau_O)}{\bar{\dot{m}}_O} \\
& + \left\{\left(\frac{1}{\bar{r}+1}\right) - \frac{1}{2}\frac{\bar{r}}{\bar{T}_C}\overline{\frac{\partial T_C}{\partial r}}\right\}\frac{\dot{m}'_F(t-\tau_F)}{\bar{\dot{m}}_F} \ .
\end{aligned}$$

(86)

Where for the perturbation in chamber pressure:

$$P'_C(t) = P_C(s)e^{st} \ , \ \frac{d}{dt}P'_C(t) = sP_C(s)e^{st} \ .$$

(87), (88)

For the perturbation oxidizer flow rate:

$$\dot{m}'_O(t) = \dot{M}_O(s)e^{st} \ ,$$

$$\dot{m}'_O(t-\tau_O) = \dot{M}_O(s)e^{s(t-\tau_O)} \ , \ \frac{d}{d(t-\tau_O)}\dot{m}'_O(t-\tau_O) = s\dot{M}_O(s)e^{s(t-\tau_O)} \ .$$

(89), (90), (91)

And, for the perturbation fuel flow rate:

$$\dot{m}'_F(t) = \dot{M}_F(s)e^{st} \ ,$$

$$\dot{m}'_F(t-\tau_F) = \dot{M}_F(s)e^{s(t-\tau_F)} \ , \ \frac{d}{d(t-\tau_F)}\dot{m}'_F(t-\tau_F) = s\dot{M}_F(s)e^{s(t-\tau_F)} \ .$$

(92), (93), (94)

Substituting equations 87, 88, 90, 91, 93, and 94 into equation-86 gave the characteristic equation:

$$\tau_C s + 1 = f_O(s) Y_O(s) e^{-s\tau_O} + f_F(s) Y_F(s) e^{-s\tau_F} . \tag{95}$$

Where the injector admittances for the oxidizer and fuel were given by:

$$Y_O(s) = \frac{\dot{M}_O(s)\,\overline{P}_C}{P_C(s)\,\overline{\dot{m}}_O} , \quad Y_F(s) = \frac{\dot{M}_F(s)\,\overline{P}_C}{P_C(s)\,\overline{\dot{m}}_F} . \qquad (96), (97)$$

For the oxidizer and fuel gains:

$$f_O(s) = \begin{cases} \left(\dfrac{\overline{r}}{\overline{r}+1}\right) & : \text{constant gas temperature assumed} \\ \left(\dfrac{\overline{r}}{\overline{r}+1}\right) + \left(\tau_C s + \dfrac{1}{2}\right) \dfrac{\overline{r}}{\overline{T}_C} \overline{\dfrac{\partial T_C}{\partial r}} & : \text{fluctuating gas temperature assumed} \end{cases} , \tag{98}$$

$$f_F(s) = \begin{cases} \left(\dfrac{1}{\overline{r}+1}\right) & : \text{constant gas temperature assumed} \\ \left(\dfrac{1}{\overline{r}+1}\right) - \left(\tau_C s + \dfrac{1}{2}\right) \dfrac{\overline{r}}{\overline{T}_C} \overline{\dfrac{\partial T_C}{\partial r}} & : \text{fluctuating gas temperature assumed} \end{cases} . \tag{99}$$

Dividing equation-95 by the left-side and then multiplying equation-95 by the denominators of both $Y_O(s)$ and $Y_O(s)$ as given by equations 64 and 65, gave:

$$\left(\alpha_{33} + A^*\right)\left(\beta_{33} + B^*\right) = f_O C^* E^* \left(\beta_{33} + B^*\right) + f_F D^* F^* \left(\alpha_{33} + A^*\right) . \tag{100}$$

Where:

$$A^* = \frac{\alpha_{11}\alpha_{23}\alpha_{32}}{\alpha_{21}\alpha_{12} - \alpha_{11}\alpha_{22}} , \quad B^* = \frac{\beta_{11}\beta_{23}\beta_{32}}{\beta_{21}\beta_{12} - \beta_{11}\beta_{22}} , \qquad (101), (102)$$

$$C^* = \gamma_3 , \; D^* = \delta_3 , \; E^* = \frac{e^{-s\tau_O}}{\tau_C s + 1} , \; F^* = \frac{e^{-s\tau_F}}{\tau_C s + 1} . \qquad (103), (104), (105), (106)$$

The characteristic equation, equation-100 was re-written as:

$$\alpha_{33}\beta_{33} + a\alpha_{33} + b\beta_{33} = c . \tag{107}$$

Where for the coefficients a, b, and c:

$$a = B^* - f_F D^* F^* \ , \ b = A^* - f_O C^* E^* \ ,$$

(108), (109)

$$c = f_O C^* B^* E^* + f_F D^* A^* F^* - A^* B^* \ .$$

(110)

The characteristic equation, equation-107 was split into the real and imaginary portions. For the real portion:

$$C_1 R_{3O} R_{3F} + C_2 R_{3O} + C_3 R_{3F} + C_4 = 0 \ .$$

(111)

For the imaginary portion:

$$D_1 R_{3O} R_{3F} + D_2 R_{3O} + D_3 R_{3F} + D_4 = 0 \ .$$

(112)

Where for the coefficients C_1, C_2, C_3, and C_4 :

$$C_1 = \lambda^2 - \omega^2 \ ,$$

(113)

$$C_2 = \left(\lambda \xi_F - \omega \eta_F\right) + \left(a_R \lambda - a_I \omega\right) \ ,$$

(114)

$$C_3 = \left(\lambda \xi_O - \omega \eta_O\right) + \left(b_R \lambda - b_I \omega\right) \ ,$$

(115)

$$C_4 = \left(\xi_O \xi_F - \eta_O \eta_F\right) + \left(a_R \xi_O - a_I \eta_O\right) + \left(b_R \xi_F - b_I \eta_F\right) - c_R \ .$$

(116)

And for the coefficients D_1, D_2, D_3, and D_4 :

$$D_1 = 2\lambda\omega \ ,$$

(117)

$$D_2 = \left(\lambda \eta_F + \omega \xi_F\right) + \left(a_R \omega + a_I \lambda\right) \ ,$$

(118)

$$D_3 = \left(\omega \xi_O + \lambda \eta_O\right) + \left(b_R \omega + b_I \lambda\right) \ ,$$

(119)

$$D_4 = \left(\xi_O \eta_F + \eta_O \xi_F\right) + \left(a_R \eta_O + a_I \xi_O\right) + \left(b_R \eta_F + b_I \xi_F\right) - c_I \ .$$

(120)

Where from equations 108, 109, and 110:

$$a = a_R + j a_I \ , \ b = b_R + j b_I \ , \ c = c_R + j c_I \ .$$

(121), (122), (123)

For the oxidizer feed system:

$$\xi_O = L_{3O}\left(\lambda^2 - \omega^2\right) + \frac{K_{i3O}}{C_{3O}} \ , \ \eta_O = 2 L_{3O} \lambda \omega \ .$$

(124), (125)

For the fuel feed system:

$$\xi_F = L_{3F}\left(\lambda^2 - \omega^2\right) + \frac{K_{i3F}}{C_{3F}} \quad , \quad \eta_F = 2L_{3F}\lambda\omega \; .$$

(126), (127)

Solving equations 111 and 112 for R_{3O} gave:

$$R_{3O} = -\left(\frac{C_3R_{3F} + C_4}{C_1R_{3F} + C_2}\right) = -\left(\frac{D_3R_{3F} + D_4}{D_1R_{3F} + D_2}\right) \; .$$

(128)

Solving equation-128 for R_{3F} gave:

$$E_1R_{3F}^2 + E_2R_{3F} + E_3 = 0 \; ,$$

(129)

$$R_{3F} = \frac{1}{2E_1}\left(-E_2 \pm \sqrt{E_2^2 - 4E_1E_3}\right) \; .$$

(130)

Where for E_1, E_2, and E_3 :

$$E_1 = C_3D_1 - C_1D_3 \; ,$$

(131)

$$E_2 = C_3D_2 - C_2D_3 - C_1D_4 + C_4D_1 \; ,$$

(132)

$$E_3 = C_4D_2 - C_2D_4 \; .$$

(133)

Once R_{3F} was determined, it was substituted into equation-128 to determine R_{3O}. The scaled resistances R_{3O} and R_{3F} were defined as:

$$R_{3O} = 2\frac{\left(\overline{P}_{3O} - \overline{P}_C\right)}{\overline{P}_C} \quad , \quad R_{3F} = 2\frac{\left(\overline{P}_{3F} - \overline{P}_C\right)}{\overline{P}_C} \; .$$

(134), (135)

The scaled resistances given by equations 134 and 135 are twice the scaled pressure drops across the oxidizer and fuel injectors elements. For a given frequency range and single value of damping coefficient, a curve of $R_{3O}/2$ vs. $R_{3F}/2$ may be generated. For a non-zero damping coefficient, if the curve passes through the operating point of the injector, then the frequency will correspond to the chamber pressure oscillations and the damping coefficient will give the damp time. A negative damping coefficient will correspond to chamber pressure oscillations that will decay with time. A positive damping coefficient will correspond to chamber pressure oscillations that will grow with time. A zero damping coefficient will correspond to the neutral stability boundary, where chamber pressure neither grow or decay.